

Geostatistical Analysis and Mitigation of the Atmospheric Phase Screens in Ku-Band Terrestrial Radar Interferometric Observations of an Alpine Glacier

Simone Baffelli, *Student Member, IEEE*, Othmar Frey, *Senior Member, IEEE*, Irena Hajnsek, *Fellow, IEEE*

Abstract—Terrestrial Radar Interferometry (TRI) can measure displacements at high temporal resolution and potentially with high accuracy. An application of this technique is the observation of surface flow velocity of steep, fast flowing glaciers. For these observations, the main factor limiting the accuracy of TRI observations is the spatial and temporal variability in the distribution of atmospheric water vapor content, causing a phase delay (Atmospheric Phase Screen, (APS)) of a magnitude comparable to the displacement signal. This contribution presents a geostatistical analysis of the spatial and temporal behavior of the APS in Ku-Band terrestrial radar interferometry. The analysis bases on the assumption of a separable spatio-temporal covariance structure, which is tested empirically using variogram analysis. From this analysis, spatial and temporal APS statistics are derived and used in a two-step procedure combining regression-Kriging with generalized least squares (GLS) inversion to estimate a velocity time-series. The performance of this method is evaluated by cross-validation, using observation of stable scatterers. This analysis shows a significant reduction in residual phase variance compared to the commonly employed approach, combining linear models of APS stratification and interferogram stacking.

I. INTRODUCTION

A. Motivation

AVALANCHING glaciers [1], [2] can pose a hazard to alpine valleys. Ice calving at their terminus can have major consequences, both directly through the subsequent ice avalanche, and indirectly, as the falling ice mass can start other event as floods, snow avalanches and debris flows, sometimes with severe consequences. The 1956 disaster at the Mattmark dam construction site [3], the 1962 and 1967 Mount Huascaran avalanches and the 2002 Kazbek massif debris flow [4] are examples of the hazards of these types of glaciers [1].

Recent advances in the understanding of glacier failures [1] suggest the possibility of early detection of developing glacier failures for two classes of avalanching glaciers. In the case of steep, unbalanced cold glaciers, such as in the Weisshorn hanging glacier [2], [5], [6], mechanical instabilities in the ice are the main mechanisms leading to break-off events, where the rupture happens within the ice mass. A log-periodic oscillation of the surface velocity superimposed to a power-law acceleration is observed in these cases [6]. This behavior may reveal useful to predict break-off times if frequent observations of the surface velocity are available. In the second class of steep, temperate glaciers, sliding is the main source of

instability conducive to break offs. Sub-glacial water pressure reduces basal friction, causing a major portion of the tongue to become unstable [7] and eventually to break off, such as in the case of the Allalingsletscher responsible for the 1956 Mattmark disaster. In this latter type of glacier, the surface velocity increases during *active phases*, notably in summer [1]. However, these patterns only rarely correlate with break-off events; surface velocity measurements alone are not sufficient and must be combined with other methods such as seismic measurements [8].

For both glacier types, reliable and precise measures of surface velocities are necessary to monitor them and improve the understanding of their dynamics. In this sense, area-wide estimates at high temporal resolution and over long periods of time are particularly useful. Remote sensing techniques [9]–[11] are frequently employed for glacier flow measurements, using visible and infrared images [12]–[14] or coherent [15]–[19] and incoherent [17], [20] methods with spaceborne and terrestrial [21]–[25] synthetic aperture radar (SAR) data.

In this context terrestrial radar interferometry [21]–[25] (TRI) is complementary to the more established space- and airborne SAR observations. While the spatial coverage of the former is normally smaller, these systems offer great flexibility in the acquisition geometry and timing, both of which are necessary for the surveillance and study of the fast dynamics of avalanching glaciers. Moreover, one strength of radar data is independence from external illumination and the ability to image through fog and clouds, permitting continuous observations during night and with cloud cover.

Among coherent techniques, the most useful for glacier monitoring is differential radar interferometry (D-InSAR) [26], which uses the sensitivity of the phase of microwaves to the length of the propagation path from the sensor to the observed surface. By computing the difference of phase measurements at subsequent times, D-InSAR can estimate displacements with a precision theoretically limited by the wavelength employed by the radar.

Temporal variations in the spatial distribution of the atmospheric water vapor content causing time-varying heterogeneity in the propagation speed of light are one of the largest source of errors in displacement estimation with differential radar interferometry —both in the spaceborne and in the terrestrial case— These nuisances are known as Atmospheric Phase Screen (APS) [27]–[29].

Precise estimation of displacements with D-InSAR requires phase calibration to remove—or at least mitigate—the phase contribution caused by the APS.

This task has been extensively studied for spaceborne InSAR, but in smaller measure for TRI observations, owing to the relative scarcity of such data sets. The different acquisition geometry and the short revisit times frequently employed in these cases suggest a reevaluation of common APS correction strategies, since these were originally developed for spaceborne InSAR.

B. State of the Art

The atmosphere is a complex, dynamic object: temporal fluctuations of temperature, pressure and water vapor content [30] and their heterogeneous spatial distribution produce spatial and temporal variations in the atmospheric refraction index. These variations in propagation speed are the causes of the APS in differential radar interferometry.

Complementary observations are sometimes employed to model the distribution of refractivity at the time of the acquisitions and hence correct the phase delays in interferometric observations. Examples of external observations are weather model outputs [31] and wet zenith delays (WZD) maps derived from Global Navigation Satellite System (GNSS) observations [27], [32]–[34] or from spaceborne microwaves radiometers and imaging spectrometers [35]–[38].

In most cases, APS estimation methods base on a combined model of the atmospheric phase screen, partitioning its variability [39], [40] between a deterministic component a stochastic contribution.

The first component is a phase screen of low spatial frequency, attributed to vertical stratification [31], [41]–[48], often observed to correlate with terrain relief. The random contribution is attributed to turbulent mixing of water vapor in the troposphere. The turbulent component shows a complex behavior in time and space and cannot be modeled deterministically. Because the APS is correlated in space, it is described through its spatial covariance or semivariance functions [29], [30], [32], which in some cases are derived from turbulence theory [30], [49].

The turbulent contribution is frequently assumed to be uncorrelated in time [39], [50], [51]. Thanks to this assumption, the APS separated from other sources of phase nuisance and from the deformation phase using time series analysis applied on a set of scatterers whose phase response is stable in time, the so-called persistent scatterers [52]. These point-wise estimates of the APS are then extrapolated to a regular grid covering the area of interest using geostatistical interpolators such as Kriging [50], [53], which account for its spatially correlated nature. The extrapolated APS can then be subtracted from the interferometric phase observations, which are then processed to estimate the displacement signal [54], [55].

C. Research Gaps

These solutions are primarily applicable to spaceborne InSAR: in the terrestrial case the spatial extent of the scene

can be much smaller than the resolutions of external weather models.

Moreover, in TRI only a portion of the atmospheric air column is traversed, while the auxiliary data acquired from space would give the total phase delay through the entire height of the troposphere. However, similar concepts employing automatic weather station (AWS) data exist for TRI [44], [56]. Unfortunately, such observations are often not available during a TRI monitoring campaign. Even if this data is acquired, these approaches can only correct large-scale, low frequency phase variations and cannot compensate local phase heterogeneities of high spatial frequency.

These limitations suffered by external observations motivates the development of APS correction approaches based only on the statistical behavior of the APS, which operate exclusively on radar data.

However, the applicability of the statistical assumptions used in spaceborne D-InSAR to TRI is doubtful because of the smaller spatial coverage of the data and the peculiar acquisition geometry, very different to the one of spaceborne SAR.

In the TRI case, the radar signal only travels through a small vertical portion of the troposphere, while in spaceborne SAR the entire atmospheric air column is traversed. Because of this, both the deterministic models of stratified APS and of the statistical model of turbulence derived for spaceborne InSAR may not apply to TRI observations.

The smaller scene size, the shorter vertical propagation path and—in the case of observation of fast displacements—the short time interval between acquisitions in TRI reduce the effect of atmospheric stratification as well. This in turn reduces the performance of APS stratification models in the TRI case.

With respect to the turbulent APS, the statistical assumptions of temporal uncorrelatedness has to be assessed considering the shorter revisit times often used in TRI.

D. Contributions of This Paper

This work presents a geostatistical analysis of the atmospheric phase screen [27]–[29] (APS) affecting Ku-Band TRI data with the aim of studying the research gaps discussed above. To do so, the study starts from an APS model similar to the one customarily employed in InSAR studies, assuming a combination of turbulent and stratified atmosphere. Using this mathematical setup, several issues are investigated:

- 1) The performance of several models for APS stratification is assessed statistically by measuring their ability to describe the phase variance observed at a set of persistent scatterers (PS). These points are chosen at locations known to be only affected by atmospheric disturbances.
- 2) The assumption of spatially correlated, temporal uncorrelated statistics, which is commonly used to model the APS in spaceborne InSAR data is replaced by a separable spatio-temporal covariance model. The suitability of this model is tested with variogram analysis.
- 3) The performance of APS correction using a regression-Kriging interpolator accounting for stratification effects and a spatial covariance model of turbulence is evaluated.

Its performance is measured by computing the residual phase variance at a set of non-moving PS.

- 4) A time-series inversion approach employing the temporal covariance model is presented. Its performance in mitigating the residual APS observed after regression-Kriging correction is assessed.

II. METHODS

A. Differential Radar Interferometry: Signal Model

Differential radar interferometry [57], [58] uses the phase coherency exhibited by radar images: the phase of a scatterer acquired by a coherent radar contains a contribution proportional to the line-of-sight distance from the sensor to the object. Therefore, the phase difference computed from a pair of images taken at different times contains a contribution proportional to the displacements of the scatterers composing the scene.

More precisely, consider a radar placed at a fixed location where the origin $\mathbf{0}$ of a Cartesian coordinate system is set. Consider a scatterer located at \mathbf{s} at time t_k ; its phase measured by the above radar is:

$$\phi(t_k) = \frac{4\pi}{\lambda} R(t_k) + \phi_{scat}(t_k) + \phi_{atm}(t_k) \quad (1)$$

where $R = |\mathbf{s}|$ is the distance between scatterer and sensor and ϕ_{scat} is the scattering phase, which depends on dielectric properties, shape of the object and to a radar-specific phase offset due to delays in the electronics and cables, λ is the wavelength and finally ϕ_{atm} is the excess phase delay caused by the atmosphere.

On scatterer moving with velocity $v = \frac{\Delta R}{t_{l+m} - t_l}$ along the line of sight (LOS) in a period of duration Δt between times t_l and t_{l+m} the *interferometric phase* or *interferometric phase difference* is:

$$\begin{aligned} \Delta\phi &= \frac{4\pi}{\lambda} \Delta R + 2\pi n + \epsilon_{atm} + \epsilon_{decorr} \\ &= \frac{4\pi}{\lambda} \Delta t v + 2\pi n + \epsilon_{atm} + \epsilon_{decorr} \end{aligned} \quad (2)$$

where Δt is often called the *temporal baseline*; the term $2\pi n$ indicates that phase measurements are ambiguous modulo half the wavelength, $\epsilon_{atm} = \phi_{atm}(t_{l+m}) - \phi_{atm}(t_l)$ represents the additional differential phase delay due to changes in atmospheric refraction index and ϵ_{decorr} describes the noise-like phase error due to thermal noise in the radar and to changes ϕ_{scat} due to variations the scatterer's properties.

Equation (2) shows that the interferometric phase difference is sensitive to the displacement ΔR but also to changes in the dielectric properties of the imaged objects and to changes in the propagation medium. In differential interferometry, the objective is the estimation of the displacement ΔR (or the velocity v) from noisy phase observations; therefore all terms but the displacement are considered nuisances. To improve the displacement estimation robustness—and possibly to estimate an object's displacement history—, multiple phase measurements at different times are often used. Thus, the model describing a single interferometric phase observation of (2) is extended to multiple observations as follows:

Given a vector \mathbf{y} of PN radar phases $y(i, l)$ derive from single look complex data (SLC) acquired at N times t_k and P locations \mathbf{s}_i , estimate the (PN) -element vector \mathbf{v} of surface velocities $v(i, l)$ at times $t_l = \frac{t_k + t_{k+1}}{2}$ with $0 < k < N$ between subsequent acquisitions and at locations \mathbf{s}_i with $0 < i < P$ [59], [60].

In analogy to (2), it is convenient to replace the SLC phase vector \mathbf{y} with the PM -dimensional vector of interferometric phases \mathbf{z} :

$$\mathbf{z} = \bar{\mathbf{A}}\mathbf{y} \quad (3)$$

where \mathbf{z} is a PM -dimensional vector of phase differences at P locations and M times. Here M is the number of interferograms, which can be at most $\frac{N+1}{2}$, the number of unique pairs that can be formed from N SLC images. The matrix $\bar{\mathbf{A}} = \mathbf{I}_P \otimes \mathbf{A}$ is the incidence matrix; a $MP \times NP$ block-diagonal matrix used to compute the interferometric phases from the SLC phase vector. Each of its blocks \mathbf{A} indicates which of the N acquisitions are paired to form interferograms in \mathbf{z} : entries A_{mk} and A_{ml} are -1 and 1 for the m -th interferogram between the l -th and the k -th acquisition. For example, given $N = 4$ SLC images, the matrix \mathbf{A} used to compute the three unique interferograms between successive acquisitions is:

$$\mathbf{A} = \begin{bmatrix} 1 & -1 & 0 & 0 \\ 0 & 1 & -1 & 0 \\ 0 & 0 & 1 & -1 \end{bmatrix}. \quad (4)$$

The (PN) -element vector of velocities \mathbf{v} can be related to the vector of interferometric phases [30], [39], [59], [60] in analogy with (2):

$$\mathbf{z} = \bar{\mathbf{B}}\mathbf{v} + \epsilon_z. \quad (5)$$

Where $\bar{\mathbf{B}} = \mathbf{I}_P \otimes \mathbf{B}$ and \mathbf{B} is a $M \times N$ matrix of the time spans between the acquisition times of the SLC images used to compute \mathbf{z} . Its construction from the interferogram incidence matrix \mathbf{A} is described in [59]. As an example, using the incidence matrix \mathbf{A} of equation (4) and assuming regularly spaced acquisitions with Δt seconds separation, \mathbf{B} will be:

$$\mathbf{B} = \begin{bmatrix} \Delta t & 0 & 0 & 0 \\ 0 & \Delta t & 0 & 0 \\ 0 & 0 & \Delta t & 0 \end{bmatrix}. \quad (6)$$

Finally, ϵ_z is a term subsuming all the noise-like contributions, assumed to be a zero-mean Gaussian random process with a $PM \times PM$ covariance matrix Σ_z , describing the spatial and temporal correlation of the nuisance terms.

As the noise is assumed to be drawn from a multivariate Gaussian distribution of known covariance, the generalized least squares (GLS) solution of equation (5) is the minimum variance, unbiased estimator for \mathbf{v} [61], [62] :

$$\hat{\mathbf{v}} = (\bar{\mathbf{B}}^T \Sigma_z^{-1} \bar{\mathbf{B}})^{-1} \bar{\mathbf{B}}^T \Sigma_z^{-1} \mathbf{z}. \quad (7)$$

In many cases, acquisitions too distant in time cannot be used to form interferograms because they would show a too high level of phase noise caused by temporal decorrelation and will be affected by excessive phase wrapping. In this case, \mathbf{A} will only consists of those rows where the temporal baseline is shorter than a given threshold, thus $M < \frac{(N)(N-1)}{2}$

and the rank of \mathbf{B} is deficient. In this case the problem is underdetermined and there is no unique solution for \mathbf{v} . An example of this situation is shown in equation (6), where only three interferograms are available to estimate four parameters.

The problem of decorrelation can be mitigated by adopting approaches based on persistent scatterers (PS), where only observations at highly coherent scatterers [50], [52], [63] unaffected by temporal decorrelation are used for the inversion. These methods are of limited use when the surface flow velocity of glaciers is studied, since the continuously changing surface features and the rapid motion make the detection of PS very unlikely. As an alternative, the rank of (5) can be increased by using a simplified velocity model, described by a vector \mathbf{p} with a smaller number of parameters $d < PN$ [59]:

$$\mathbf{v} = \mathbf{M}\mathbf{p} \quad (8)$$

For example, assuming constant velocity v_0 over time, the model for the i -th pixel is:

$$\mathbf{v}_i = \begin{bmatrix} v_0 \\ \vdots \\ v_0 \end{bmatrix} = \mathbf{I}_{N,1} v_0 = \mathbf{M}_i \mathbf{p} \quad (9)$$

and \mathbf{M} is the block-diagonal matrix $\mathbf{I}_{N,1} \otimes \mathbf{I}_{N,P}$.

\mathbf{M} can be any $PN \times d$ matrix describing a simplified spatial and temporal displacement model and possibly imposing spatio-temporal smoothness constraints.

Thus, the problem is rewritten as:

$$\mathbf{z} = \bar{\mathbf{B}}\mathbf{M}\mathbf{p} + \epsilon_z = \bar{\mathbf{G}}\mathbf{p} + \epsilon_z. \quad (10)$$

Where the *design matrix* $\bar{\mathbf{G}}$ is written with a bar to indicate that it is the design matrix for the whole set of P pixels in the set of all M interferograms. For simplicity $\bar{\mathbf{G}}$ is assumed to be a block matrix with P blocks \mathbf{G} —the same velocity model is assumed for each pixel and no spatial constraints are set—

The GLS estimate of \mathbf{p} is obtained with:

$$\hat{\mathbf{p}} = (\bar{\mathbf{G}}^T \Sigma_z^{-1} \bar{\mathbf{G}})^{-1} \bar{\mathbf{G}}^T \Sigma_z^{-1} \mathbf{z}. \quad (11)$$

The variance of the estimates is given by:

$$\text{var}(\hat{\mathbf{p}}) = \bar{\mathbf{G}}^T \Sigma_z^{-1} \bar{\mathbf{G}}. \quad (12)$$

Without further assumptions, the covariance matrix of the nuisance, Σ_z must only be positive-semidefinite. As the APS is known to be spatially correlated and can potentially show temporal correlations, its inversion can be computationally very costly [39].

However, by making certain assumptions that will be discussed later, the spatially correlated contributions in Σ_z can be estimated and removed before the least-squares inversion. By doing so, a new data set is obtained, where the APS is approximately uncorrelated in space, making the inversion computationally easier.

Whether the full inversion is attempted or the latter approach is used, knowledge of the covariance matrix of the interferogram network is required for the inversion and to provide uncertainty estimates for the derived parameter. As the interferometric phases \mathbf{z} are derived from the SLC phases via (3),

the interferogram covariance is related to the covariance of the SLC phase vector \mathbf{y} [39]:

$$\Sigma_z = \bar{\mathbf{A}} \Sigma_y \bar{\mathbf{A}}^T. \quad (13)$$

ϵ_y is [30], [39]:

$$\epsilon_y = \epsilon_{y,atm} + \epsilon_{y,decorr}, \quad (14)$$

where $\epsilon_{y,atm}$ is the phase contribution from the atmospheric phase screen and $\epsilon_{y,decorr}$ represents the phase noise due to the effect of temporal decorrelation in each acquisition. These two terms are assumed to be mutually uncorrelated because they are produced by different physical mechanisms; therefore they can be written a sum of separate terms. When discussing the SLC phase, the noise terms must be seen as deviations from the noise-free SLC phases consisting only of the propagation term and the intrinsic scattering phase as in (1) [39]. These equations are only a tool to model the covariance of the interferometric phases. By linearity, the same decomposition applies to the covariance matrix of the interferometric phase vector Σ_z :

$$\Sigma_z = \Sigma_{z,atm} + \Sigma_{z,decorr}. \quad (15)$$

The following sections are dedicated to the individual covariance terms.

1) *Covariance of Decorrelation Phase Noise:* $\Sigma_{z,decorr}$ models the effect of thermal noise in the measurement system and random changes in reflectivity on the stability of the observed interferometric phases. This is usually quantified through the magnitude of the interferometric phase coherence, γ [64] derived from spatial or temporal multilooking by assuming ergodicity [65]. The coherence magnitude is used to estimate the interferometric phase variance through the Cramer-Rao lower bound [66]. The phase variance for a interferogram pixel located at \mathbf{s}_i at time $t_l = \frac{t_o + t_p}{2}$, derived from acquisitions at times t_o and t_p is:

$$\text{Var}[z_{i,o,p}] \geq \frac{\sqrt{1 - \gamma_{i,o,p}^2}}{\gamma_{i,o,p} \sqrt{2L}}. \quad (16)$$

where the notation $\gamma_{i,o,p}$ indicates the coherence estimate at pixel i from acquisitions o and p .

In the case considered here, with interferograms acquired at zero spatial baseline, the decorrelation noise is spatially uncorrelated. $\Sigma_{z,decorr}$ is a block-diagonal matrix, where each $M \times M$ block represents the covariance of the decorrelation process for an individual pixel [39]. In this work, the temporal covariance $\Sigma_{z,decorr}(i)$ for the i -th pixel is assumed to follow the Brownian decorrelation model. This is derived assuming the displacement of each scatterer composing a resolution cell to be drawn from a uniform distribution at any time [39], [64], [67]. This model creates an exponential decay in coherence between acquisitions:

$$\gamma(\Delta T) = \gamma_0 e^{-\frac{\Delta T}{\tau}}. \quad (17)$$

The Brownian motion model is not suitable to model decorrelation for all types of terrain; it was found to be applicable to urban areas in [67]. In many cases the coherence shows more

complex patterns such as seasonal trends or variations correlated with weather conditions. These cases are not modeled in this work.

2) *Covariance of Atmospheric Phase Screen*: The term $\epsilon_{y,atm}$ models the phase delay caused by the inhomogeneous distribution of atmospheric water vapor in the scene [27]–[29]. Its effect can not be appreciated in the SLC phase, only in interferograms: temporal changes in the spatial distribution of atmospheric delay $\epsilon_{y,atm}$ between acquisitions are revealed in the interferometric phase difference as low spatial frequency atmospheric phase screens.

Part of the spatial phase trends can be approximated using linear models by assuming homogeneous or layered distributions of atmospheric water vapor [31], [41]–[48]. These models are often not sufficient to capture the full APS phase variability and must be augmented with a statistical description. Thus, the APS is written as the superposition of these terms [39], [40]:

$$\epsilon_{y,atm} = \epsilon_{y,atm, strat} + \epsilon_{y,atm, turb}. \quad (18)$$

where $\epsilon_{y,atm, strat}$ is the *stratified* APS and $\epsilon_{y,atm, turb}$ is the *turbulent* APS, due to turbulent mixing in the troposphere [30], [32], which is modeled statistically as a zero mean random process with covariance matrix $\Sigma_{y,atm}$.

More precisely, the random process generating the APS can be described through a covariance matrix $\Sigma_{y,atm}$ if and only if its covariance function C is *stationary* in space and time. This means that C depends only the spatial separation $\mathbf{d} = \mathbf{s}_1 - \mathbf{s}_2$ and on the temporal lag $t = t_1 - t_2$, not on the locations themselves [68]. This assumption is frequently accompanied by the one of *isotropy* in space, where C does not depend on the direction of \mathbf{d} but only on its magnitude $d = |\mathbf{d}|$.

In spaceborne InSAR studies, the APS covariance is further simplified by assuming lack of temporal correlation [39], thus:

$$C(d, t) = C_s(d) \delta(t). \quad (19)$$

Where $\delta(t)$ is the Dirac delta function. The assumption of uncorrelatedness in time is justifiable because in spaceborne InSAR the acquisition repetition times are in the order of days, where it is reasonable to expect that the turbulent behavior in troposphere changed completely.

This assumption is a particular case of the more general property of *separability* which is assumed in this work. A separable covariance function C can be factorized in the product of temporal and spatial covariances:

$$C(d, t) = C_t(t) C_s(d). \quad (20)$$

Separability implies that the spatial statistics are not a function of time; this is a very stringent assumption, which is seldom entirely applicable. As an example, it is violated by *Taylor's hypothesis* [28], [29], [33], [34], [68]–[70]. In the latter, it is assumed that turbulent eddies are transported by a mean wind field \mathbf{v} which does not change their structure. Therefore, the temporal covariance function can be written as a function of the spatial covariance and of the velocity field:

$$C_t(\mathbf{d}, t) = C_s(\mathbf{d} - \mathbf{v}t). \quad (21)$$

Despite its limitations, separability is very useful as it greatly simplifies fitting statistical models; more practically, it greatly reduces the size of covariance matrices.

Consider the APS covariance matrix of the SLC phase vector—the discrete form of the covariance function in (20)—. In the stationary, separable case, this matrix can be written as a Kronecker product of a $P \times P$ spatial covariance matrix $\Sigma_{y,atm,s}$ and of a $N \times N$ temporal covariance matrix $\Sigma_{y,atm,t}$ [39], [71]:

$$\Sigma_{y,atm} = \Sigma_{y,atm,s} \otimes \Sigma_{y,atm,t}. \quad (22)$$

Using (13) the APS covariance matrix of the interferogram vector is:

$$\begin{aligned} \Sigma_{z,atm} &= \bar{\mathbf{A}} \Sigma_{y,atm} \bar{\mathbf{A}}^T = \\ &= (\mathbf{I} \otimes \mathbf{A}) (\Sigma_{y,atm,s} \otimes \Sigma_{y,atm,t}) (\mathbf{A}^T \otimes \mathbf{I}^T) = \\ &= \Sigma_{y,atm,s} \otimes (\mathbf{A} \Sigma_{y,atm,t} \mathbf{A}^T) \end{aligned} \quad (23)$$

where the last step follows from the mixed product property of the Kronecker product.

In summary the considerations made above, together with the assumption of spatio-temporal separability lead to the following APS model:

- 1) Assuming the APS in the SLC phase vector to have a separable covariance, the APS in the interferogram vector has separable covariance as well. The estimation and correction of the spatially and temporally correlated components can be performed separately.
- 2) The turbulent APS contribution in the interferogram phase vector has the same spatial covariance matrix as the *unobservable* APS in the SLC phase vector. The covariance does not depend on the acquisition times.
- 3) If a linear model is used to describe the stratified APS in the SLC phase, the stratified APS observed in an interferogram can be described by a functionally identical model with different model parameters.

3) *Inversion Strategy*: To summarize the findings of the previous sections, ϵ_z , the noise affecting the interferograms is assumed to be a zero-mean Gaussian random vector with covariance:

$$\Sigma_z = \Sigma_{y,atm,s} \otimes (\mathbf{A} \Sigma_{y,atm,t} \mathbf{A}^T) + \Sigma_{z,decorr} \quad (24)$$

where $\Sigma_{y,atm,s}$ is the $P \times P$ matrix of the spatial APS covariance, $\Sigma_{y,atm,t}$ the $N \times N$ matrix of the temporal APS covariance and $\Sigma_{z,decorr}$ is the $PM \times PM$ diagonal or block-diagonal matrix of the decorrelation phase noise. Finally, each interferogram is affected by a stratified APS, which is assumed to be deterministic and is predicted by a linear model of stratification.

The following procedure is used to estimate the APS affecting the interferogram vector and to reconstruct \mathbf{p} :

- For each interferogram l at time t_l an estimate $\hat{\epsilon}_{z,atm}(t_l)$ of the spatially correlated APS is obtained by regression-Kriging interpolation of the interferometric phases observed on a set of persistent scatterers (PS) whose phase should not be affected by displacements. These estimates are subtracted from the interferogram vector \mathbf{z} , reducing

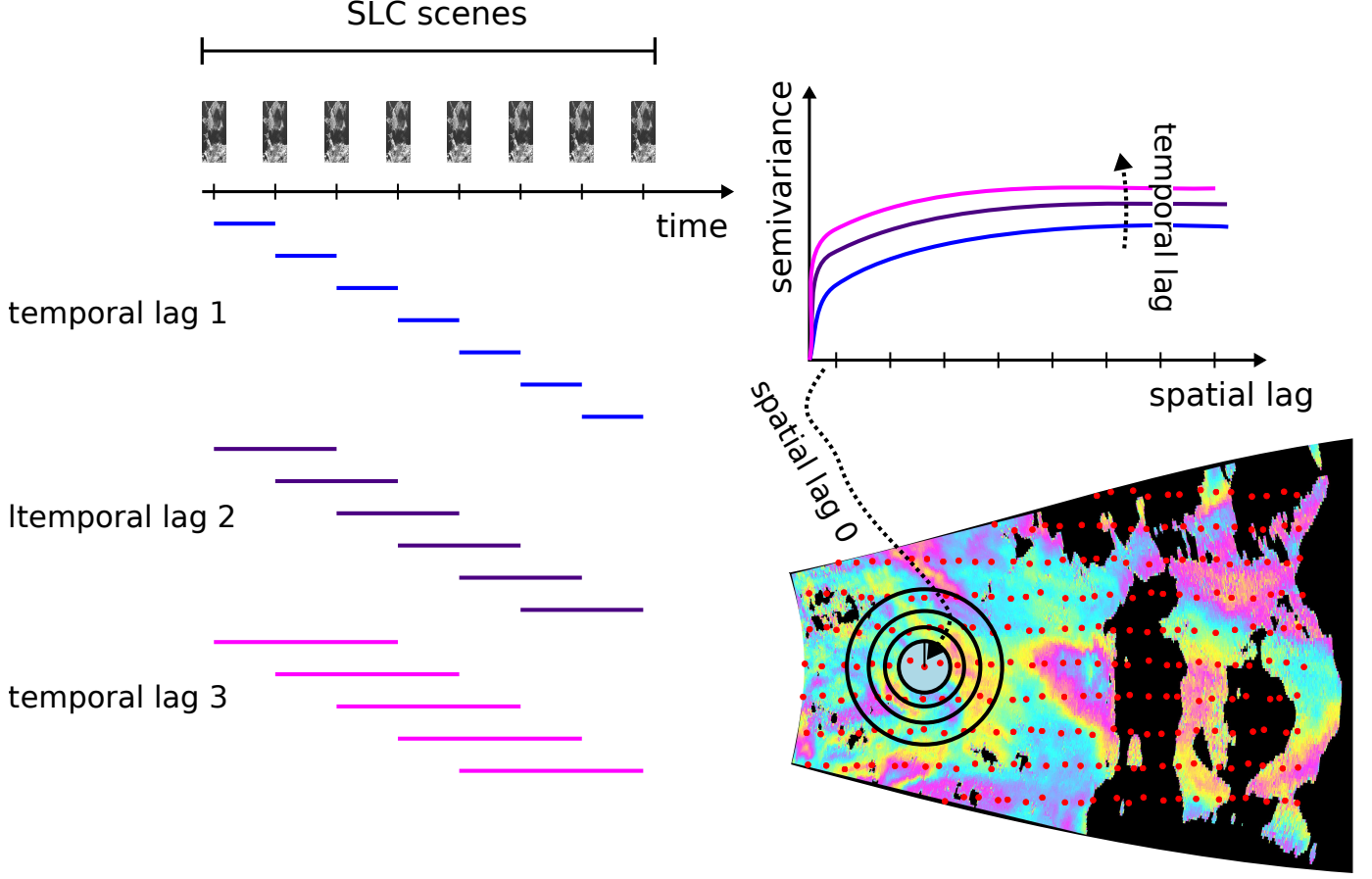


Fig. 1: Illustration of the computation procedure for the spatio-temporal variogram, used to estimate the space-time covariance of the APS, $\Sigma_{y,atm}$. Assuming separability, the spatial covariance of the APS has the same structure as the covariance of the interferograms and can be estimated as the spatial variogram averaged over all temporal baselines. The temporal variogram corresponds to the mean phase variance of the interferogram grouped by temporal lags.

the spatial correlation in the residual interferogram vector \mathbf{z}_{res} to an extent where it can be assumed to be negligible.

- The generalized least squared inversion for \mathbf{p} can then be performed on the residual interferogram vector \mathbf{z}_{res} independently for each pixel, provided that the design matrix \mathbf{G} can be written as a block-diagonal matrix with P blocks and assuming each pixel i to be affected by a spatially uncorrelated, temporal correlated APS and decorrelation noise contribution, which is assumed to have a covariance matrix:

$$\begin{aligned} \Sigma_{z,res}(i) &= \Sigma_{z,t}(i) = \\ \mathbf{I} \otimes (\mathbf{A}\Sigma_{y,atm,t}\mathbf{A}^T) &+ \Sigma_{z,decorr}(i). \end{aligned} \quad (25)$$

The correction of the spatially correlated contribution $\epsilon_{y,atm,s}$ will be described in detail in subsection II-B, while the pixel-wise GLS inversion to obtain estimates of the displacement parameters is discussed in subsection II-C.

A block diagram showing the general principle of the employed APS correction and inversion scheme is shown in Fig. 2. The next sections will be devoted to the discussion of the various steps used in this approach.

B. Spatial Correction of APS

1) *Regression-Kriging*: According to the model setup, the interferometric phase $z(i, l)$ at time t_l and any location \mathbf{s}_i is written as the superposition of displacement phase and stratified and turbulent APS:

$$\begin{aligned} z(i, l) &= \\ z_{disp}(i, l) + \epsilon_{z,atm}(i, l) &= \\ = z_{disp}(i, l) + \epsilon_{z,atm,strat}(i, l) + \epsilon_{z,atm,turb}(i, l) \\ = z_{disp}(i, l) + \mathbf{X}\beta(l) + \epsilon_{z,atm,turb}(i, l) \end{aligned} \quad (26)$$

where \mathbf{X} is a matrix of regressors, which are either functions of the coordinates \mathbf{s}_i or measurement of auxiliary variables at the same positions. $\beta(l)$ is the vector of unknown stratified APS parameters at time t_l and $\epsilon_{z,atm,turb}$ is the turbulent APS.

The parameter vector $\hat{\beta}(l)$ of the stratified APS model can be estimated given prior information on the distribution of displacement throughout the scene, which is easily inferred in the case of TRI monitoring of fast moving alpine glaciers: the area undergoing displacement is of limited spatial extent and often surrounded by features such as mountain flanks and rocks that are effectively immobile relative to the flow of the

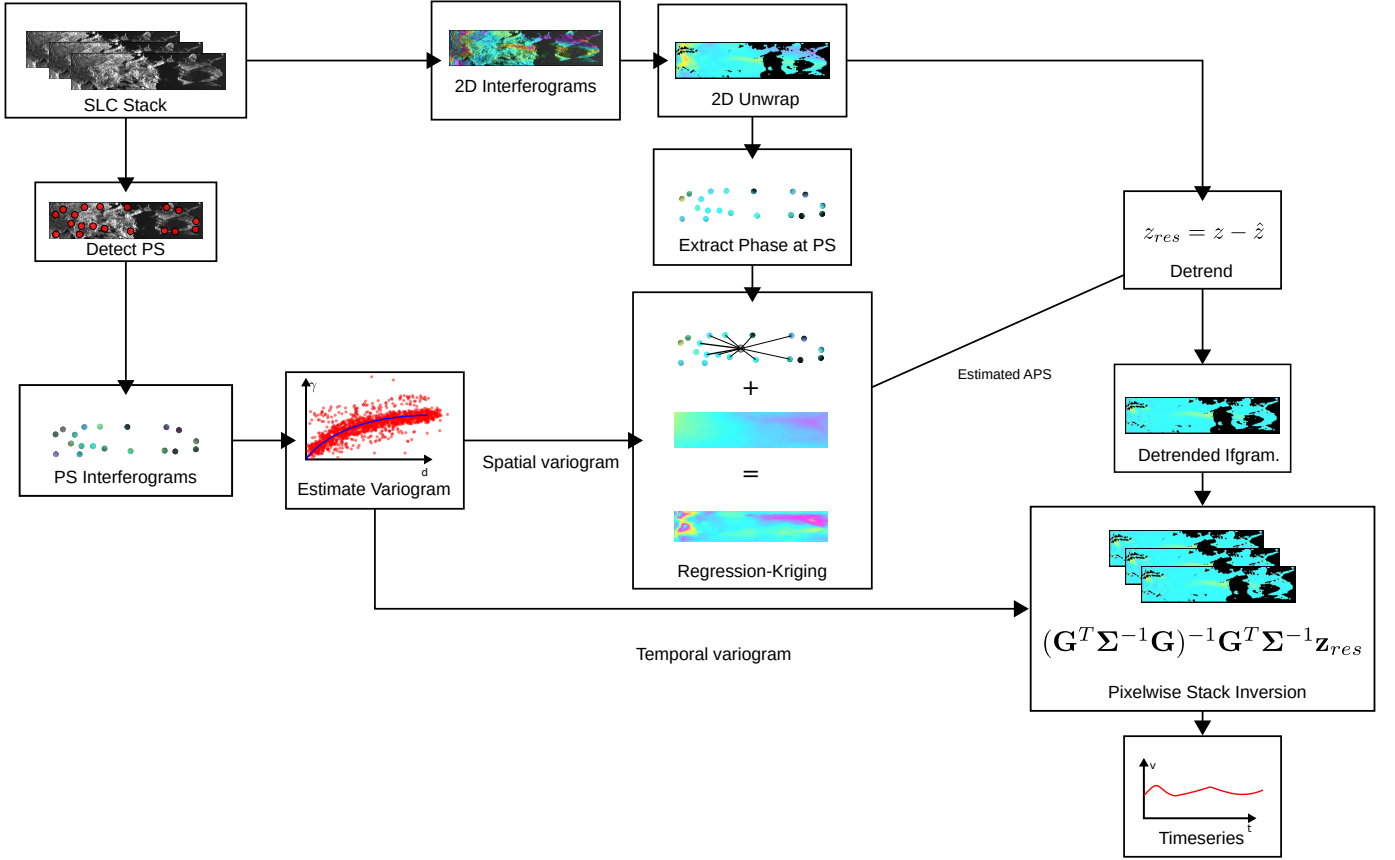


Fig. 2: Schematic description of the two-step spatial APS mitigation and time-series inversion.

glacier—which can be in the order of meters per days in the case studied in this paper—

To estimate $\hat{\beta}$ a subset S of persistent scatterers (PS) from the P pixels in the interferogram is used; it is assumed that their phase at any time only consist of the stratified and turbulent APS contributions, with spatial covariance $\Sigma_{z,atm,s}^{PS}$. The best linear unbiased estimator of $\beta(l)$ is given by the GLS estimator [72]–[74]:

$$\hat{\beta}(l) = \left(\mathbf{X} \Sigma_{z,atm,s}^{PS} \mathbf{X}^T \right)^{-1} \Sigma_{z,atm,s}^{PS} \mathbf{X}^T \mathbf{z}(j, l). \quad (27)$$

where \mathbf{X} is the matrix of regressors at locations $\mathbf{s}_j, j \in \mathbf{S}$, $\mathbf{z}(j, l)$ the vector of PS phases and $\Sigma_{z,atm,s}^{PS}$ is the spatial covariance of the APS between the PS locations. Using $\hat{\beta}$, the stratified APS contribution at any pixel i in the interferogram can be predicted:

$$\hat{\epsilon}_{z,atm,stat}(i, l) = \mathbf{X}(i, l) \hat{\beta}(l). \quad (28)$$

However using (28) does not give predictions for the turbulent component of the APS, which is often the dominant source of phase variability in the interferograms. Due to the spatial correlation of the APS, it is reasonable to assume that the turbulent APS at a location \mathbf{s}_i near a PS observation $\mathbf{s}_j, j \in \mathbf{S}$ is similar to the phase residual—measured phase minus GLS prediction of stratification—of (27) at that PS:

$$\epsilon_{res}^{PS}(j, l) = z(j, l) - \mathbf{X}(j, l) \hat{\beta}(l). \quad (29)$$

The similarity should decrease with increasing distance from the PS as the spatial correlation decreases with spatial separation.

A time l , the turbulent APS at \mathbf{s}_i can be approximated as a weighted average of the GLS residuals ϵ_{res}^{PS} at the available PS $\mathbf{s}_j, j \in \mathbf{S}$,

$$\hat{\epsilon}_{z,atm,turb}(i, l) = \mathbf{w}(l) \epsilon_{res}^{PS}(l) \quad (30)$$

where \mathbf{w} is a weight vector which is a function of the distances between \mathbf{s}_i and $\mathbf{s}_j, j \in \mathbf{S}$. Under these conditions, the minimum variance, unbiased estimator for the turbulent APS is given by the Kriging equation [53], [72]:

$$\hat{\epsilon}_{z,atm,turb}(i, l) = \mathbf{v}^T \Sigma_{res}^{PS-1} \epsilon_{res}^{PS} \quad (31)$$

where \mathbf{v} is the vector of spatial APS covariances between $z(i, l)$ and $z(j, l), j \in \mathbf{S}$ and Σ_{res}^{PS} is the covariance matrix of the regression residuals at the PS.

The predictor of the combined deterministic and turbulent APS at any point \mathbf{s}_i is then the *regression Kriging* estimator:

$$\hat{\epsilon}_{z,atm,s}(i, l) = \mathbf{x}(i, l) \hat{\beta}(l) + \mathbf{v}^T \Sigma_{res}^{PS-1} \epsilon_{res}^{PS} \quad (32)$$

A similar approach is presented in [75], where intrinsic random functions of order k (IRF- k) [76] are used to predict the spatially correlated APS contribution from observations at a set of PS locations. This method is similar to regression Kriging [77], [78], with the difference that in the form presented in [75] external regressors cannot be employed [78].

In practice, only the nearest K PS to any prediction point s_i are used in order to speedup the inversion of Σ_{res}^{PS-1} . This is justifiable since the farther an observation is located to a reconstruction point, the smaller its weight will be. Furthermore, when the APS is extrapolated to the entire interferogram, the Kriging prediction is computed on a grid whose spacing is larger than the interferogram pixel spacing, the gaps are filled using a distance-weighted bilinear interpolator.

2) *Selection of Stratified APS Model*: The choice of a model for the stratified APS component according to (28) deserves separate consideration. Homogeneity and isotropy of the atmospheric refraction index distribution are commonly assumed in the case of terrestrial interferometry, where the scene is often of limited size [41]. These assumptions predict an APS proportional to the range distance from the radar [24], [41]–[43], [47]. To account for spatial inhomogeneities in water vapor distribution, other authors propose polynomial models of higher order, usually restricted to second order [42].

In situations with large variations in terrain height, the assumption of homogeneous atmospheric refraction index is not suitable; in these cases atmospheric layering is modeled as a height dependent component added to the above homogeneous model [45]–[47]. These model mostly account for the variation in atmospheric density with increasing elevation, frequently known as the *hydrostatic delay*.

An alternative approach is to use weather parameters [44], [56] to model variations of the atmospheric refraction index. However, given the large vertical extents expected when monitoring steep alpine glaciers, from which significant vertical temperature and water vapor gradients can be expected and which are not included in the models, and because no precise weather data is available, these models are not considered in this study.

The models described in this section are summarized in Table I. In the table, the variable r represents the slant range from the radar, while h is the elevation and θ is the azimuth angle. The selection of a stratified APS model best fitting the measurement data is made according to an automatic procedure: The interferometric phases at the PS for a large set of interferograms are used to compute ordinary least squares (OLS) fit for each model. The fitting is repeated for each of the available interferograms. The relative performance of the models is evaluated comparing the distribution of the Akaike Information Criterion (AIC) [80] and of R^2 for the models over the set of interferograms.

It must be remembered that the model fit used in model comparison are obtained with ordinary least squares (OLS) and not with the optimal minimum variance GLS estimator of (27). This approximate shortcut seems reasonable since the purpose of this analysis is comparison of the relative performance of models.

3) *Spatial Covariance Model For Turbulent APS*: Computing the regression-Kriging prediction according to (32) requires knowledge of \mathbf{v} , which is derived from covariance of the APS between two points in space s_i, s_j . Theoretical considerations from turbulence theory [30], [33], [34], [49], [70], [81] and data derived from GNSS or spaceborne SAR observations [29], [32], [49] are often employed to derive APS

spatial structure functions [82] —variograms, correlograms or periodograms— from which the covariance can be determined or approximated.

Nonetheless, the validity of these covariance models in the TRI case is uncertain, given the small number of studies available, the large variability in acquisition setups and scene choice and also due to the fact that the imaging geometry specific to TRI is very different to the one in spaceborne InSAR studies. Thanks to the assumption of spatio-temporal separability and isotropy, the spatial covariance function can be estimated from the data using a variogram estimator:

$$\gamma_s(d) = \frac{1}{2|N(d)|M_{PS}} \sum_{l=0}^{M_{PS}} \sum_{(i,j) \in N(d)} |z(j,l) - z(i,l)|^2 \quad (33)$$

where the sum index l runs over M_{PS} interferograms at different temporal baselines. For each interferogram the mean square phase difference between all PS with spatial separation d , given by the index set $N(d)$ is computed. Since z is the interferometric phase difference at a fixed location, the empirical spatial variogram estimator corresponds to the mean squared *double phase difference* —single difference in time and double difference in space— over the set of all interferograms.

To reduce the estimation bias caused by the stratified component of the APS in z [83] the variogram γ_s is estimated using on OLS estimation residuals of the stratified model [72].

From this empirical spatial variogram γ_s , a variogram model is fitted using a nonlinear fitting procedure; the variogram model is used to obtain an approximation $\hat{\mathbf{v}}$ of the covariance between observations and test points, which can be used for the Kriging predictor. If a bounded spatial variogram model $\gamma_{s,m}$ can be fit to the empirical variogram estimate, the value of the spatial covariance function at any spatial lag is computed with [74]:

$$C_s(d) = \gamma_{s,m}(\infty) - \gamma_{s,m}(d). \quad (34)$$

Where $\gamma_{s,m}(\infty)$ is the variogram sill, the value that the variogram attains at infinite spatial separation between samples, which corresponds to the phase variance of the interferograms. If spatial statistics of the APS are estimated from the data, it is advisable to strive for a spatially homogeneous distribution of PS, such that a homogeneous distribution of lags d between PS locations is achieved, ensuring a reliable estimate of the spatial variogram.

The imaging geometry of TRI should also be considered. Due to the limited aperture size the images are acquired in a polar geometry. Thus, the data matrix as returned by the radar is defined on a polar grid in the range-azimuth plane (r, θ) . For this type of sampling the spatial lag d between two points must be determined using the distance formula for polar coordinates and not with the euclidean distance normally used in most geostatistics packages.

In this paper a more convenient approach is chosen: the data is geocoded using a digital elevation model. The variograms are estimated on the geocoded data, which is now resampled in 3D Cartesian coordinates, where the true distance between points is easily determined. This is relevant in scenes with

Name	Trend	Comments	References
Unprocessed	$\phi = \beta_0$	No atmospheric trend is modeled; included for performance comparison.	-
Linear	$\phi = \beta_0 + \beta_1 r$	Assumes homogeneous, isotropic atmospheric refraction index. This model is applicable with little topography and small height extents, where no stratification is expected.	[41]–[43]
Quadratic Range	$\phi = \beta_0 + \beta_1 r + \beta_2 r^2$	Models inhomogeneities of refraction index as a linear trend in range.	[24], [42]
Height dependent I	$\phi = \beta_0 + \beta_1 r + \beta_2 r h$	Assumes a horizontally isotropic and homogeneous troposphere with vertical layers [79], resulting in an exponential dependence of refraction index with height, which is approximated to the first order.	[45], [46]
Height dependent II	$\phi = \beta_0 + \beta_1 r + \beta_2 h^2$	Similar assumptions as <i>Height Dependent I</i> , here the horizontal and vertical components of refraction are considered to be separable.	[47]
Quadratic 2D Range	$\phi = \beta_0 + \beta_1 r + \beta_2 \theta + \beta_3 \theta r + \beta_4 r^2 + \beta_5 \theta^2$	Includes a lateral component describing inhomogeneity of the atmospheric conditions due to the wide field of view of the real aperture radar imaging geometry. This model is purely empirical.	
Quadratic 2D Height	$\phi = \beta_0 + \beta_1 h + \beta_2 \theta + \beta_3 \theta r + \beta_4 h^2 + \beta_5 \theta^2$	Analogous to “Quadratic 2D Range” but replacing the slant range with elevation.	

TABLE I: Summary of stratified APS models employed in terrestrial radar interferometry.

large variations in elevation, because distances in the slant-range azimuth grid could substantially differ from the ground distance between points. This difference can hinder fair comparisons of empirical variograms with theoretical covariance or semivariance functions derived from turbulence theory.

C. Temporal Inversion

1) *Temporal Covariance Model*: Even after removing the APS estimate from the interferogram vector, considerable phase variability in time is observed in the residual interferometric phases [84], [85]:

$$z_{res}(i, l) = z(i, l) - \hat{\epsilon}_{z,atm,s}(i, l) \quad (35)$$

where $\hat{\epsilon}_{z,atm,s}$ is the regression-Kriging prediction of the spatially correlated APS, whose estimation is detailed in subsection II-B.

Caudff [84] reported residual phase variations after correcting the APS by interpolating the spatially low-pass filtered phase observations of stable areas, a method similar to the Kriging interpolation proposed in subsection II-B but which does not use the spatial covariance structure of the APS in the prediction. In that case, the residual phases were observed to correlate with variation in the solar radiation.

Similar observations were made by Butt in [75], where after interpolating the APS observed at a set of PS using IRF-K, a significant residual phase error was observed, especially for

areas with a low density of PS. This was explained through the short correlation length of the APS in space and its high temporal frequency.

Under the separable covariance model described in subsection II-A, the residual APS in $z_{res}(i, l)$ is a realization of a Gaussian random process $\epsilon_{z,atm,t}$ with no spatial correlation and a temporal correlation matrix $\Sigma_{z,t}$, approximately the sum of a block diagonal matrix of APS and of a block diagonal or diagonal matrix of noise contributions due to temporal decorrelation, as described in (25):

$$\Sigma_{z,res} \approx \mathbf{I} \otimes \Sigma_{z,atm,t} + \Sigma_{z,decorr,t}. \quad (36)$$

This formulation is not exact because of the sparse distribution of the PS across the scene and the approximated covariance obtained from the variogram; a residual spatial correlation of the APS can be expected. The residual error will increase with increasing distance from the PS; for the sake of simplicity this aspect has not been considered in this analysis.

If the noise in the corrected interferogram vector $\Sigma_{z,res}$ is assumed to be spatially uncorrelated, it is only necessary to consider the temporal correlation of APS and decorrelation in the solution of (5). In this case, the temporal covariance structure is described a block-diagonal matrix $\Sigma_{z,res}$, the sum of the temporal APS covariance and of the decorrelation covariance (see (36)).

Since $\Sigma_{z,res}$ is a block-diagonal matrix, i.e the noise in \mathbf{z}_{res} is not correlated across pixels, the problem of (5) can be solved

separately for each of the P pixels since \mathbf{G} is a block-diagonal matrix of compatible size and shape, i.e the displacement model does not include spatial dependence across different locations.

The APS covariance $\Sigma_{z,atm,t}$ is estimated through $\Sigma_{y,atm,t}$ using an experimental temporal variogram, computed as the variance of the interferometric phases grouped by temporal baselines ΔT , as illustrated in Fig. 1:

$$\gamma_t(\Delta T) = \frac{1}{2|N(\Delta T)|N_{PS}} \sum_{l=0}^{N_{PS}} \sum_{i \in N(\Delta T)} |z(l, i)|^2 \quad (37)$$

where $N(\Delta T)$ is the set of all interferograms with temporal baseline ΔT and z is the unwrapped interferometric phase.

Estimating the temporal covariance of the APS requires the computation of interferograms covering all temporal baselines up to a reasonably long time-lag. This is needed even if only a subset of these interferograms can be effectively employed for the inversion. This requirement is not as stringent as it may seem, since only the interferometric phases at the PS are required, which can be computed efficiently and do not suffer from decorrelation.

Similarly, the decorrelation covariance $\Sigma_{z,decorr}$ can be derived from the SLC covariance matrix $\Sigma_{y,decorr}$ [86] and the incidence matrix \mathbf{A} . In this paper the approach suggested in [39] is used to generate covariance matrices for the decorrelation signal, assuming a Brownian decorrelation process:

- The interferometric coherence between two SLCs pixels $y(i, t_l)$ and $y(i, t_l + \Delta T)$ separated by a time ΔT is modeled with an exponential decay $\gamma(\Delta T) = \gamma_0 e^{-\Delta T/\tau}$. The observed coherence as a function of temporal baseline ΔT is computed by averaging interferograms with the same ΔT , giving $\hat{\gamma}(\Delta T)$. The parameters γ_0 and τ are estimated by minimizing $|\hat{\gamma}(\Delta T) - \gamma(\Delta T)|$ [67].
- The model parameters are used to generate the coherence matrix of the SLC vector, Γ . Then Γ is converted into the (incorrectly scaled) covariance matrix of the interferograms \mathbf{z} using \mathbf{A} . For a pixel i :

$$\Omega_{z,i} = \frac{1}{2} \mathbf{A} \Gamma_i \mathbf{A}^T. \quad (38)$$

- Finally, Ω_z is rescaled to a covariance matrix using the observed interferometric coherences and the expression for the interferometric phase standard deviation of (16). For the i -th pixel, the new matrix is:

$$\Sigma_{z,decorr,i} = \mathbf{D} \Omega_{z,i} \mathbf{D} \quad (39)$$

where \mathbf{D} is a diagonal matrix with the j -th entry corresponding to $\frac{\text{Var}[z_{j,i}]}{\Omega_{z,i,jj}}$.

To improve the robustness of the estimated decorrelation covariance matrix and to reduce computational load, γ_0 and τ are binned in 30 classes, the average covariance matrix for each class is used in the inversion.

2) *Pixel-wise GLS Inversion*: Thanks to the spatial correction of the APS described in subsection II-B the problem can be solved for each pixel individually using \mathbf{z}_{res} instead of \mathbf{z} to

yield the estimate $\hat{\mathbf{p}}$ for all times $t_l, l = 1 \dots M$ at each location \mathbf{s}_i :

$$\hat{\mathbf{p}}(i) = \left(\mathbf{G}^T \Sigma_{z,res}(i)^{-1} \mathbf{G} \right)^{-1} \Sigma_{z,t}(i)^{-1} \mathbf{G} \mathbf{z}_{res}. \quad (40)$$

where $\Sigma_{z,res}(i)$ indicates the i -th block of \mathbf{z}_{res} corresponding to the i -th pixel.

The feasibility and robustness of the inversion described by (40) are heavily influenced by the interplay of the available interferograms, controlled \mathbf{A} and by the employed displacement model, chosen by \mathbf{p} through the design of \mathbf{M} .

In designing \mathbf{A} for high repeat interval observations of fast-moving terrain, one must balance between computational and storage costs associated with computing and unwrapping all the possible interferometric pairs and the unreliable phase information provided by interferograms with large temporal baselines, that are prone to low coherence and phase wrapping.

A conservative choice is to combine only consecutive SLC images in an *interferogram chain* [22], [25], [87], [88] so that the reference acquisition in l -th interferogram appears again as the slave of the $l+1$ -th interferogram. In this configuration, $N-1$ unique interferograms are produced.

An interferogram chain is convenient in combination with a displacement model assuming a constant velocity i.e $\mathbf{p} = \mathbf{v}$ with \mathbf{v} a $P \times 1$ vector. In that case, phase contributions that appear only once in a master SLC and in a slave SLC cancel each other in the GLS solution, leaving only the contributions from interferograms at the beginning and end of the stack [89].

Assuming a single velocity for the entire time-series negates the purpose of high repeat-rate TRI monitoring because variations in displacement velocity over time are lost. The interferogram chain is also not suitable to estimate the full time-series of N velocities for each pixel, i.e $\mathbf{M} = \mathbf{I}_{PN,PN}$ with \mathbf{v} a PN -vector. This formulation likely results in unreliable estimates because only one noisy interferometric phase observation is available for each model parameter.

Redundancy in the form of a simpler displacement model and of more interferometric pairs can improve estimation robustness. Optimally, all possible $\frac{N(N-1)}{2}$ interferometric pairs can be used to obtain maximum likelihood (ML) estimates of $(N-1)$ unwrapped differential phases [67], [86], [90] as if they were interferograms computed from a single master acquisition. These ML-estimate can then be converted into a displacement history with $N-1$ displacement relative to a virtual master.

This method is not applicable in the case presented in this work: the number of interferograms to compute and store would be too large. Other than these technical limitations, temporal decorrelation and the fast flow of the glacier would make most of the interferograms very challenging to unwrap.

As to the latter issue, assuming a maximum velocity of $2 \frac{\text{m}}{\text{day}}$ in the fastest parts of the glacier, phase wraps can be expected for interferometric pairs with a temporal separation of approximately 6 min.

Since the data is acquired with a repeat interval of 150 s, this allows wrap-free interferograms between the l -th and the $l+1$ -th and $l+2$ -th SLC at the most. Such large displacement

velocities are not expected to be routinely observed; therefore a maximum temporal baseline of 500 s has been used. This choice should not result in displacement-induced phase wraps except for the most severe surges in glacier velocity. This interferogram network is described by the following incidence matrix:

$$\mathbf{A} = \begin{bmatrix} 1 & -1 & 0 & 0 & 0 & \dots & \dots \\ 1 & 0 & -1 & 0 & 0 & \dots & \dots \\ 1 & 0 & 0 & -1 & 0 & \dots & \dots \\ 0 & 1 & -1 & 0 & 0 & 0 & \dots \\ 0 & 1 & 0 & -1 & 0 & 0 & \dots \\ 0 & 1 & 0 & 0 & -1 & 0 & \dots \\ \vdots & \vdots & \vdots & \vdots & \ddots & & \end{bmatrix}. \quad (41)$$

The time-series is inverted using a displacement model forcing a constant velocity for a duration t_s longer than the SLC repeat interval. In this manner the interferograms can be divided into *stacks* during which the velocity is assumed constant. In this case, \mathbf{M} is:

$$\mathbf{M} = \mathbf{I}_P \otimes \begin{bmatrix} [1 & 0 & \dots & 0]_{\times N_s} \\ [0 & 1 & \dots & 0]_{\times N_s} \\ \vdots \\ [0 & \dots & 0 & 1]_{\times N_s} \end{bmatrix} \quad (42)$$

where N_s is the number of interferograms in each stack.

The GLS solution obtained with this model is a modified form of interferogram stacking [32], [34], [91], where a constant velocity for each pixel is assumed for the entire duration covered by the interferograms. In the modified model N_s velocities are estimated, using the parameter to control the balance between reliable estimates and temporal resolution. In this study $N_s = 16$ was empirically selected, corresponding to about 30 minutes.

III. DATA

A. Device: KAPRI

The data used in this work was acquired with KAPRI [92], [93] (Ku-Band Advanced Polarimetric Radar Interferometer), a fully polarimetric version of the Gamma Portable Radar Interferometer II (GPRI-II) [94]; a Ku-Band portable terrestrial radar interferometer. The radar is based on the dechirp-on-receive frequency modulated continuous wave (FMCW) architecture [95]. With a chirp bandwidth of 200 MHz a nominal distance resolution of 0.75 m is achieved. Since a windowing filter is used to suppress processing sidelobes caused by the Discrete Fourier transform (DFT) used for range compression, the effective range resolution is 0.9 m. Resolution in the direction perpendicular to line of sight is given by a 2 m-long slotted waveguide array with a half power beamwidth of 0.385° , corresponding to a ground cross-range resolution of 7 m at 1 km slant range.

B. Bisgletscher 2015 Campaign

A series of KAPRI data spanning the period between July to late August 2015 was acquired from the Domhütte mountain hut, at an altitude of 2940 m, looking at the Bisgletscher on the opposite side of the valley (see Fig. 3), covering a range of distances between 4000 m and 8000 m. At these distances, GPRI data have a cross-range resolution between 30 m and 60 m and a range resolution of approximately 0.9 m. A SLC image was acquired every 150 s; the repeat time is chosen to minimize temporal decorrelation and to avoid phase wrapping due to the rapid motion of the glaciers surface, estimated using time-lapse camera to be as large as $2 \frac{\text{m}}{\text{day}}$. The data set does not uniformly cover the duration of the measurement campaign due to a combination of technical and logistical limitations:

- 1) The radar installation used the hut's electrical power supply, consisting of solar panels supplemented by a small hydroelectric plant. During times of high activity at the hut, the radar had to be disconnected from its power supply. A buffer battery permitted to continue acquisition for approximately 6 h from the power cut-off. However, in some cases of longer interruptions this alternative supply was not sufficient to ensure continuous operation.
- 2) Nearly 200 GB of SLC data was produced every day. To provide data download and control the radar was connected to a Wi-Fi link provided by the PermaSense/X-Sense project [96]. Since this link is designed to connect a low-power sensor network, which is expected to produce a much lower daily data volume, daily transfers of the entire radar data set were not possible. Therefore, the SLC images were stored locally on a network attached storage (NAS) system connected to the radar using an local area network connection. Since only an $100 \frac{\text{MB}}{\text{s}}$ Ethernet cable was installed, the maximum daily data amount that could be transferred from the radars own storage to the NAS was still smaller than the predicted daily amount. To avoid running out of storage space on the computer controlling the radar, acquisitions were only carried out for 12 h each day, while the remaining time was dedicated to copying the data to the NAS system.

From the acquired data, a subset of data is sampled for the analysis of the APS: ten timestamps are chosen randomly from the set of acquisitions. For each of these timestamps, all SLC closer than one hour are used for the analysis. The random sampling is used to ensure that different atmospheric conditions are represented in the study since they are presumably influenced by the weather and the time of the day.

C. Data Processing

The acquired SLCs are coregistered to a common master acquisition by amplitude cross correlation, to minimize loss of coherence. Interferograms are formed by complex multiplication, followed by 5×2 multilooking. A larger range multilooking is used in order to minimize the loss of azimuth resolution, which by virtue of the acquisition geometry increases linearly with slant range distance. Interferograms are unwrapped using the minimum cost flow unwrapping algorithm and referenced

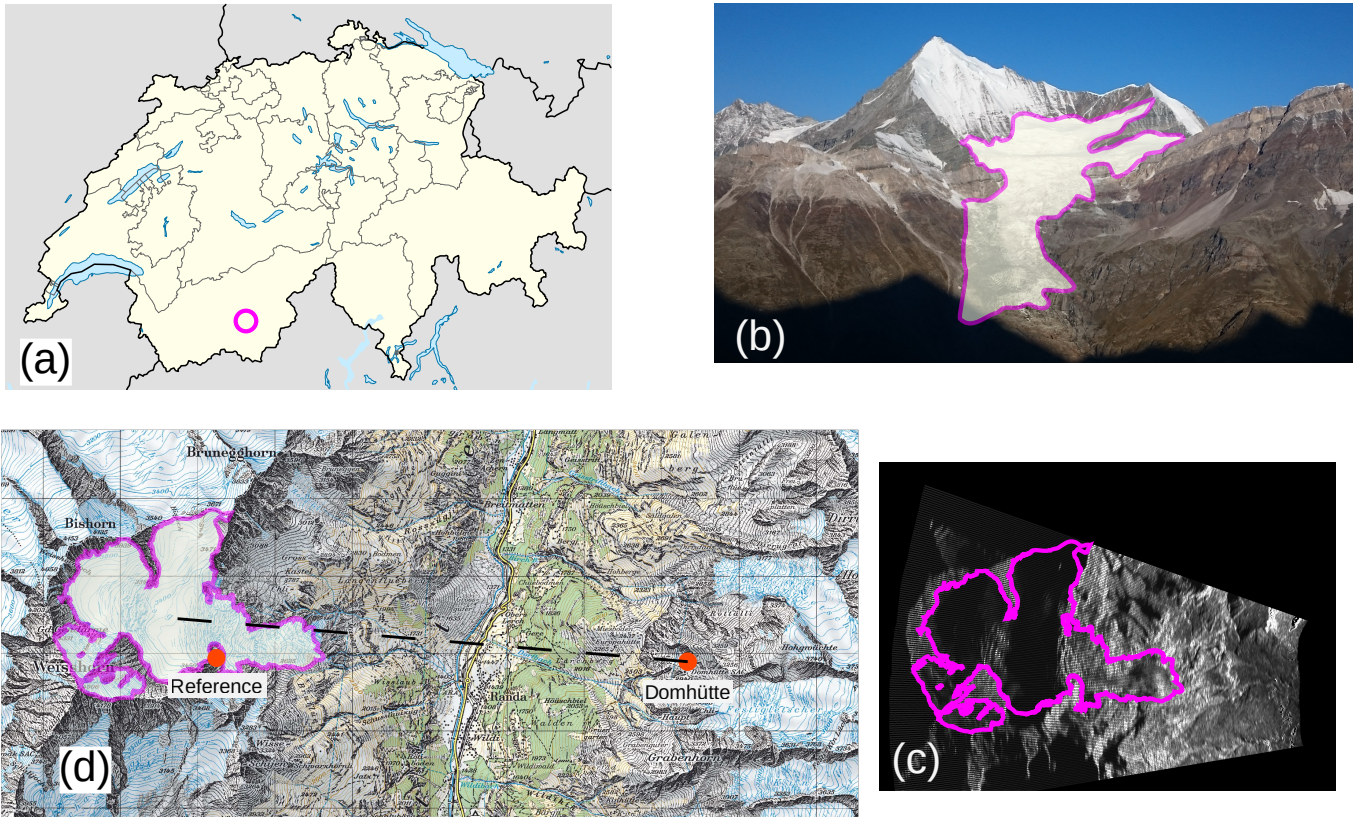


Fig. 3: Overview of the area under study. (a) Approximate location of the Bisgletscher in the Canton of Valais, Switzerland. (b) Image of the Bisgletscher as seen from the radar point of view at Domhütte, with glacier outline drawn in purple. (c) Geocoded average backscatter power map geocoded in Swiss map coordinates. (d) Locations of radar at Domhütte, glacier and reference location for interferogram referencing, overlaid on a topographic map with 1 : 50000 scale. (Basemap: [97]).

to a reference point corresponding to a stable rock face close to the glacier, as visible in Fig. 3.

The persistent scatterers used to derive spatial and temporal statistics were detected using the intensity mean to standard deviation ratio [50] on an SLC stack of 50 acquisitions and by removing the PS found in areas known to be moving. The initial list of candidate PS was reduced to an approximately homogeneous spatial PS density using the method described by [98], employing the interferometric coherence with respect to the first SLC in the stack as a quality measure. The processing chain is automated using the Nextflow [99] dataflow engine, that allows a reproducible analysis of the time-series.

IV. RESULTS

A. Spatial Correction of APS

1) *Selection of Stratified APS Model:* As discussed in subsection II-B, the phase contribution of the atmospheric phase screen in the interferograms is modeled as the sum of a deterministic delay predicted by an atmospheric stratification model and a turbulent atmospheric delay contribution, modeled as a Gaussian random variable.

In order to select the best performing linear model for the stratified APS phase $\epsilon_{z,atm,strat}$, a statistical model com-

parison is made on a large set interferograms. For each interferogram l at time t_l in the network, an ordinary least squares (OLS) estimate for $\beta(t_l)$ is computed for every linear model to be compared among those described in Table I.

The model fit parameters $\beta(t_l)$ alongside summary statistics, such as the sum of residuals, the R^2 value and the Akaike Information Criterion (AIC)[80] are stored for each model run. The results of the numerical evaluation are displayed in Fig. 4a as a boxplot of AIC values divided by model; each model is assigned a different color in the bar plot. A statistical summary of R^2 values is shown in Fig. 4b using a similar visualization.

2) *Spatial Covariance Model For Turbulent APS:* The spatial correction of the APS contribution is performed by predicting the unobserved APS at the locations of interest s according to the regression-Kriging equation (32). The estimated APS is then subtracted from the interferogram as in (35). The prediction at a point s_i requires the spatial covariance of the APS between this point and the PS used as observations. As the true APS covariance is not known, it is replaced with a covariance model derived from an experimental variogram, as illustrated by (34). The variogram is computed by averaging individual spatial variograms obtained from a number of interferograms, according to (33). These interferograms are generated using

Method	Stacking approach	Bias	Standard deviation
kriged	OLS	$-4.11 \cdot 10^{-3}$	$5.8 \cdot 10^{-2}$
kriged	APS+Coh	$-2.82 \cdot 10^{-3}$	$5.48 \cdot 10^{-2}$
kriged	Coh	$-2.67 \cdot 10^{-3}$	$5.76 \cdot 10^{-2}$
kriged	APS	$-1.99 \cdot 10^{-3}$	$5.43 \cdot 10^{-2}$
kriged	no	$-1.06 \cdot 10^{-3}$	0.26
lm	no	$1.96 \cdot 10^{-2}$	0.96
unprocessed	no	$4.9 \cdot 10^{-2}$	1.44
unprocessed	OLS	$5.04 \cdot 10^{-2}$	0.49
lm	OLS	$5.25 \cdot 10^{-2}$	0.49
unprocessed	APS	$5.38 \cdot 10^{-2}$	0.47
lm	APS	$5.62 \cdot 10^{-2}$	0.46
unprocessed	APS+Coh	$6.76 \cdot 10^{-2}$	0.47
lm	APS+Coh	$7.17 \cdot 10^{-2}$	0.47
unprocessed	Coh	$8.89 \cdot 10^{-2}$	0.47
lm	Coh	$9.74 \cdot 10^{-2}$	0.47

TABLE II: Bias and standard deviation of the residual displacement rate in $\frac{m}{day}$ extracted from a set of PS located outside of the glacier and assumed not to be undergoing displacement.

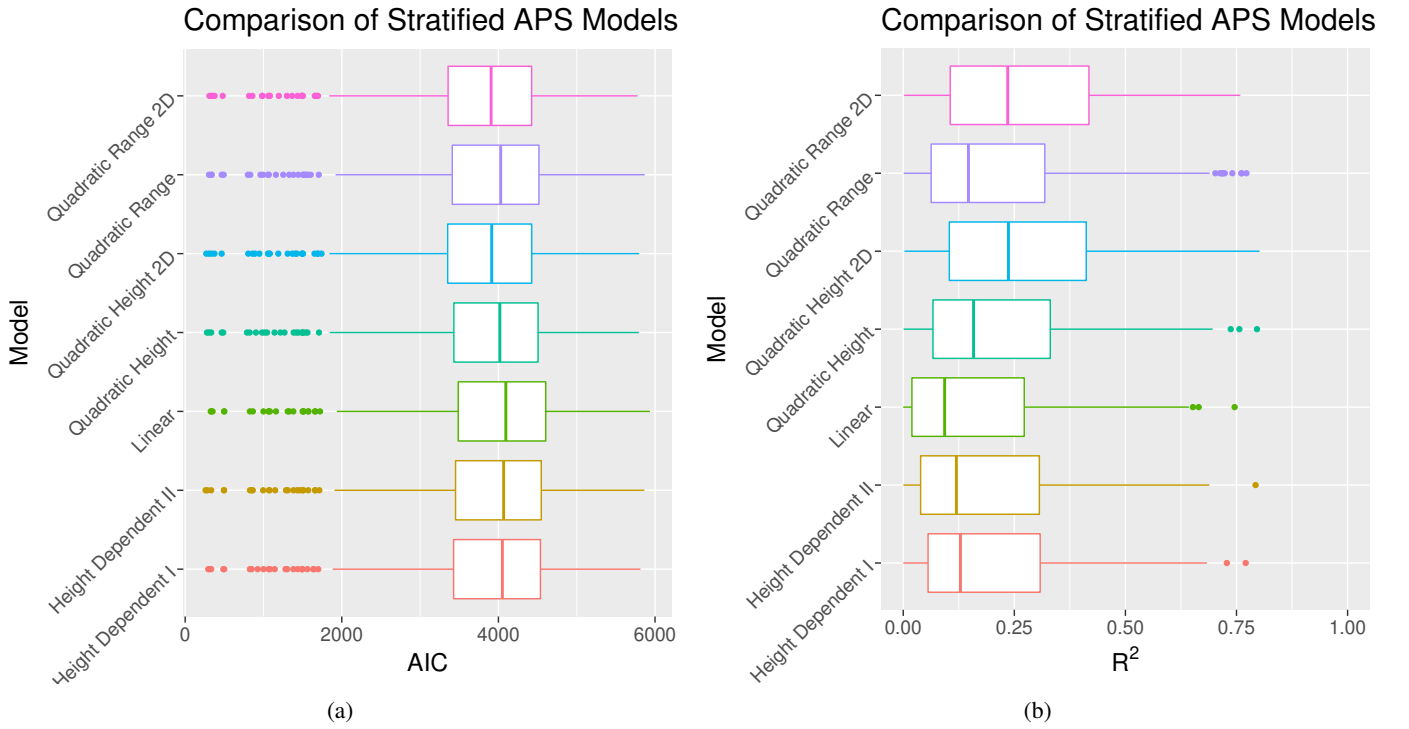


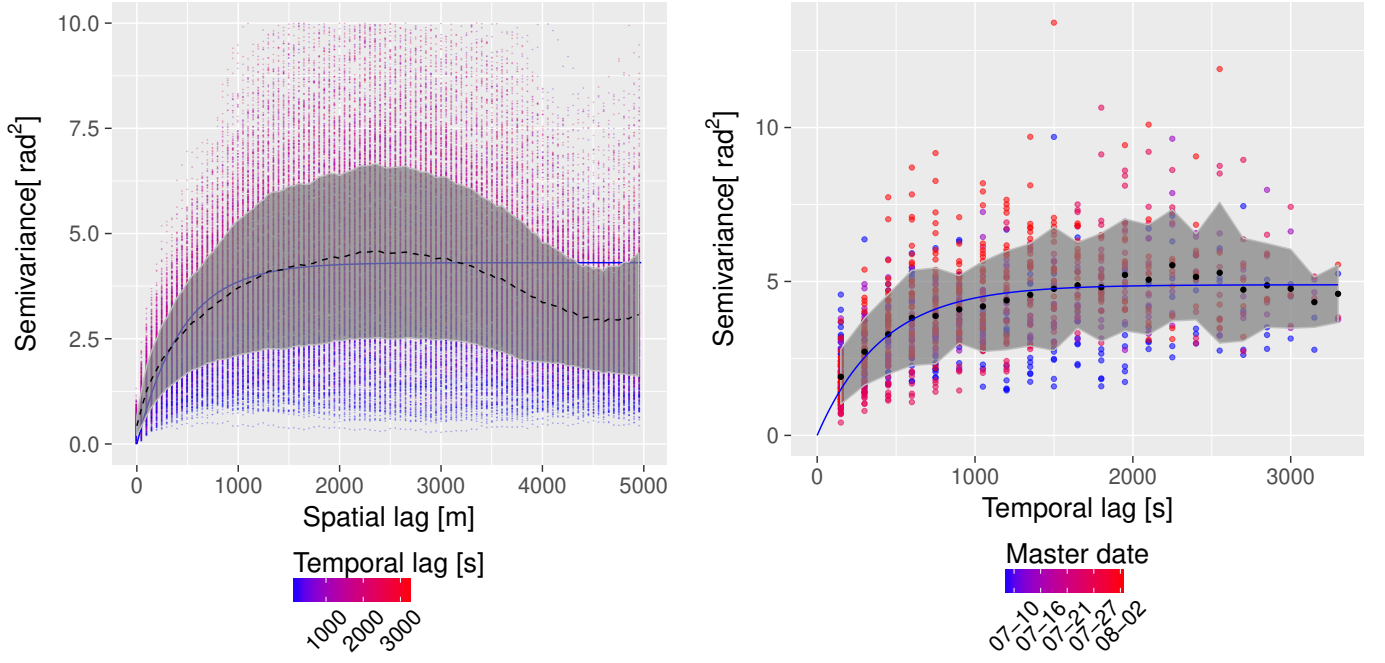
Fig. 4: (a) Boxplot of the of the Akaike Information Criterion (AIC) values for a selection of models described in Table I. To produce this figure, 508 interferograms were considered. Each of the models discussed was applied to every interferogram, the AIC statistic was computed. The AIC is plotted as a color-coded histogram, the model whose AIC is lower is the one whose performance is best relative to the other models it is compared with. (b) Boxplot of the R^2 values for the models listed in Table I. The plot is obtained with the same procedure as (a).

100 SLC acquisitions, from which all PS interferograms with a maximum temporal baseline of 120 minutes are formed.

The spatial variograms obtained from each interferogram are plotted as dots in Fig. 5a, their color encodes the temporal baseline. Assuming the validity of the separable covariance, there should be no variation in spatial covariance between interferograms; this is tested empirically by plotting the standard deviation of the spatial variograms across realizations, shown in Fig. 5a as the gray ribbon around the averaged variogram, plotted as a dashed black line. An exponential variogram model, shown as a blue line, is fitted to the average.

3) *Performance of Spatial APS Removal:* The performance of the spatial APS estimation is assessed by cross validation. A second set of PS was located on stable areas around the glacier, excluding those used to compute the RK prediction. The phases of each interferogram and the residual phase after removal of the APS estimates at these points were extracted, converted into velocities and stored.

The results of cross validation as displayed as histograms in the *no* row of Fig. 6. Three method are compared. The regression-Kriging is shown in the column labeled *kriged*. The reference case with no correction applied is displayed



(a) Empirical spatial variogram. Each dot corresponds to the empirical spatial variogram for one PS interferogram, its color indicates the temporal baseline of that interferogram. The black line is the mean variogram, surrounded by a gray ribbon showing the standard deviation of the individual variograms, while the blue line shows the fitted exponential variogram used to compute the Kriging predictions.

(b) Empirical temporal variogram, computed as the phase variance of PS interferograms with increasing temporal baselines. The color of the dots encodes the date of the master SLC used in computing that interferogram, the black dots show the mean variogram over the set of all interferograms and the gray ribbon its standard deviation. The blue line shows an exponential variogram model fit, which is used to generate temporal covariance matrices used in the inversion.

Fig. 5: Spatial and temporal variograms derived from 1535 PS interferograms computed from 100 SLC acquisitions. All possible interferogram up to a maximum temporal baseline of 120 minutes were computed and unwrapped.

in the column *unprocessed* while the results after removal of the stratified APS contribution is shown in the column labeled *lm*. The interferometric phases outside of the glacier correspond to the APS only, because on rocks no displacement is expected at the scale of the interferogram's spatial baseline. Therefore, the distribution of the estimated velocities on PS can be used as a proxy for the APS correction quality. A visual comparison of these methods, in form of standard deviation maps, is shown by the first row of Fig. 9, panels (a), (b) and (c) for the uncorrected case, the stratification model and regression-Kriging respectively. These maps are obtained with a sample estimator for the standard deviation, applied on the estimated velocity time-series.

A more quantitative assessment of the standard deviation of these residuals is given by the summary statistics Table II in the rows labeled "no". The table shows the bias and standard deviation of the displacement estimates, calculated over all times and locations.

B. Temporal Inversion

As explained in subsection II-C, it is assumed that the APS correction using regression-Kriging removes the spatial correlation of pixels; only the temporal correlation of pixels along the stack, attributed to the residual APS, described by $\Sigma_{z,atm,t}$, and the decorrelation, described by $\Sigma_{z,decorr}$,

must be considered in the GLS inversion, which can be now performed pixel by pixel.

1) *Temporal Covariance Model*: The Brownian coherence decay model parameters τ and γ_0 were computed using a subset of the interferograms. These estimates are useful to quantify the rapidity of the decorrelation process and are used to construct the covariance matrix $\Sigma_{z,decorr}$ as described in subsection II-C. The estimates of γ_0 and τ are plotted as a geocoded maps overlaid on a topographic map in Fig. 7.

The second component of the temporal covariance is the covariance of the APS; assuming spatio-temporal separability of the APS statistics $\Sigma_{y,atm,t}$ is estimated from a temporal variogram using a set of PS interferograms with increasing temporal baselines. Using this method, the variogram at lag t corresponds to the phase variance computed for all interferogram with temporal baseline t , as illustrated in Fig. 1. The resulting temporal variogram is plotted in Fig. 5b along with a curve showing the fitted exponential variogram model.

2) *Performance of Pixel-wise GLS Inversion*: The pixel-wise GLS inversion performance is tested by the same cross-validation procedure described in subsection IV-A. The phases at the same set of points described above are extracted, converted in displacement velocities and plotted in Fig. 6, in the row named *OLS*, *Coh*, *APS+Coh*, *APS* that represent four inversion approaches using different temporal covariance matrices:

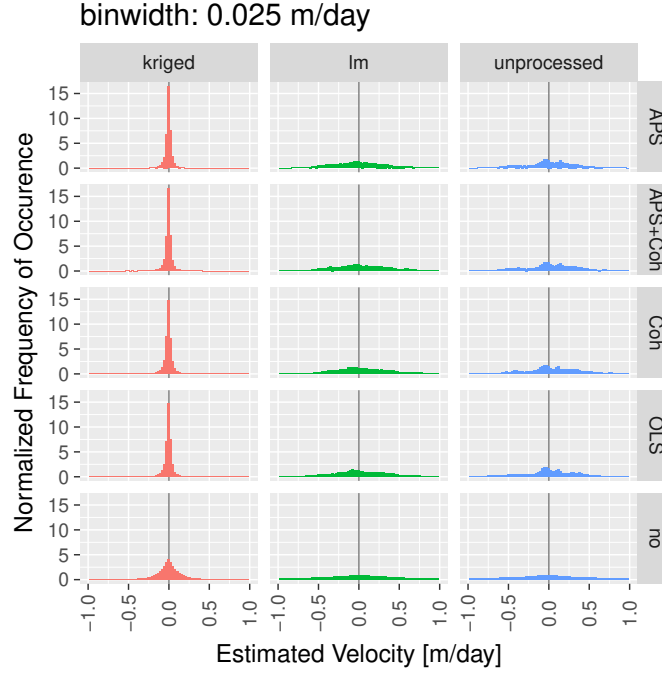


Fig. 6: Histogram of estimated velocities at non-moving location for different combinations of APS correction and time-series inversion methods.

Each column corresponds to a spatial APS correction method: *kringed* is obtained using regression-Kriging, *lm* using the stratified APS only while in the column *unprocessed* no spatial APS correction is applied. Across rows, different temporal covariance models are used for the GLS time series inversion. In *APS* only the temporal covariance of the APS is considered, in *Coh* only the covariance of the temporal decorrelation process, while *APS + Coh* uses both. In *OLS* no covariance model is used, while in *No* the interferometric phases are converted in velocities.

- OLS: Ordinary least squares inversion, the temporal covariance matrix is set to the identity matrix.
- Coh: GLS inversion, temporal covariance only includes the Brownian decorrelation model.
- APS: GLS inversion, temporal covariance only includes APS.
- APS+Coh: GLS inversion, temporal covariance according to (36).

The same plots are repeated across three columns (*Kriged*, *LM*, *unprocessed*), showing the combined effect of different spatial APS removal techniques and temporal covariance models.

The average velocity at the non-moving location is expected to be close to zero with a small variance, as they are derived from the interferometric phases of parts of the scene that do not displace significantly at the timescales of the interferograms. A larger variance indicates a larger uncorrected APS contribution or a higher level of decorrelation, causing more phase noise.

A visual representation of the estimated velocity maps is shown in Fig. 8 for a small selection of times. Three maps obtained without spatial APS correction and using a pixel-wise OLS inversion are displayed in a. The same maps obtained with regression-Kriging and a OLS inversion are shown in b. Finally, in c regression-Kriging is combined with GLS using a temporal covariance considering both APS and decorrelation. The temporal standard deviation of the estimates is plotted in Fig. 9, in panel d through i.

V. DISCUSSION

A. Spatial Correction of APS

1) *Selection of Stratified APS Model*: The stratified APS contribution is predicted by a linear model. It is hard to know *a priori* which of the models listed in Table I is the most suitable to the situation analyzed in this paper. Model selection was made using a statistical comparison, as described in subsection IV-A. Fig. 4a displays a statistical summary of the Akaike Information Criterion (AIC) values, while Fig. 4b shows a similar summary of R^2 values.

The AIC values are only meaningful in the relative sense: among the investigated models, the one with the lowest AIC will have the best fit quality, in the maximum likelihood sense [80]. As shown by the box plot in 4a, all models have a very similar distribution of the AIC values over the interferograms considered for the analysis, with the “Quadratic Height 2D” model showing the best AIC and the higher R^2 in Fig. 4b.

It appears that the very similar distributions of the AIC statistics across models could be due to multicollinearity between the slant range distance and height variables in the linear regression, which is explained by the observation geometry shown in Fig. 3: an increase in distance from the radar corresponds to increasing terrain elevations. The presence of multicollinearity is verified empirically in Fig. 10 by plotting r against h for the points used in the regression. The possibility

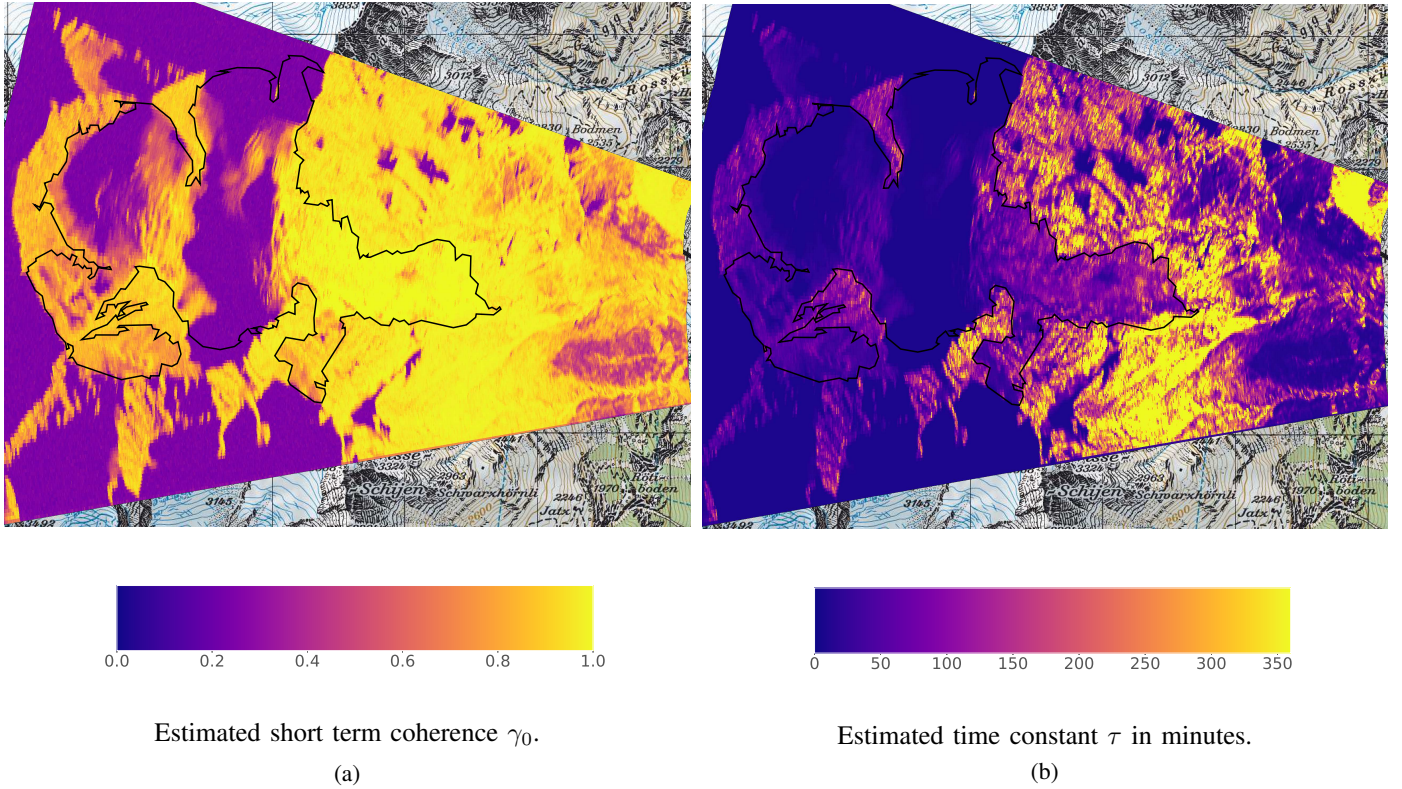


Fig. 7: Estimated short term coherence γ_0 (a) and time constant τ (b) parameters for the Brownian coherence decay model $\gamma(\Delta t) = \gamma_0 e^{-\frac{\Delta t}{\tau}}$. The data was obtained by fitting an exponential decay on average coherence maps binned by temporal baseline. The outline of Bisgletscher is shown as a black polygon. (Basemap: [97], swisstopo, outline: [100]).)

of multicollinearity seems realistic considering the correlation of r and h . In this case, either regressor can be included in the stratified APS model.

The 2D model including height and azimuth angle was chosen for regression-Kriging as it showed the highest R^2 in Fig. 4b. The inclusion of the azimuth angle presumably increases the model fit quality because it can better describe lateral variations in the APS, due to the wide field of view of the radar. Even this model only shows a median R^2 of 0.25 and an interquartile range of 0.3. This means that for most interferograms, between 80 percent and 60 percent of the total phase variability is not explained by stratification.

Considering the initial assumption of the APS being the superposition of stratification and turbulence, this results implies that a majority of phase variability should be attributed to turbulent mixing, highlighting the importance of its statistical modeling.

The relatively poor performance of APS stratification models can also be appreciated in Table II in the row where “Method” is “lm” and “Stacking Approach” is “no”. Compared to the uncorrected case, shown in the very last row of that table. The estimation standard deviation is reduced by only $0.4 \frac{\text{m}}{\text{day}}$, but is still of a magnitude comparable to the glacier’s daily displacement.

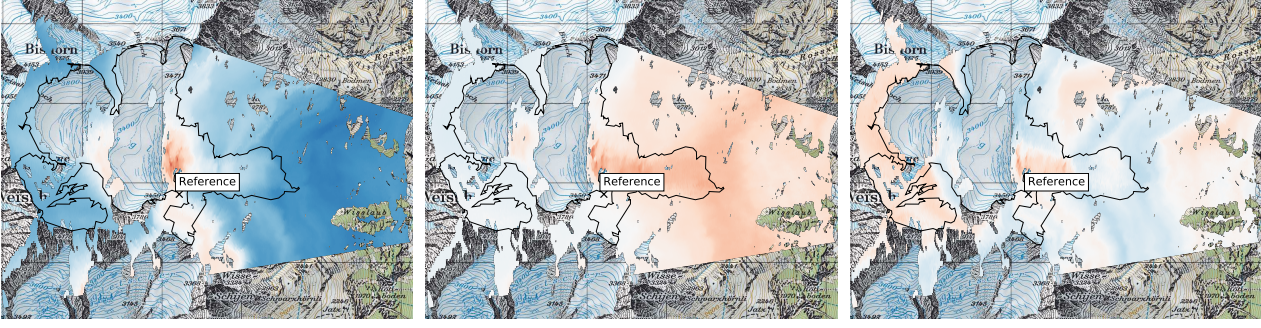
These results are in contradiction with several studies of APS correction in TRI [31], [41]–[47], [56], where a stratification model is shown to significantly reduce both bias and variance. However, these studies were sometimes performed

in less challenging environments and for the purpose of monitoring slower displacements. Hence, in most cases using a single reference interferogram network.

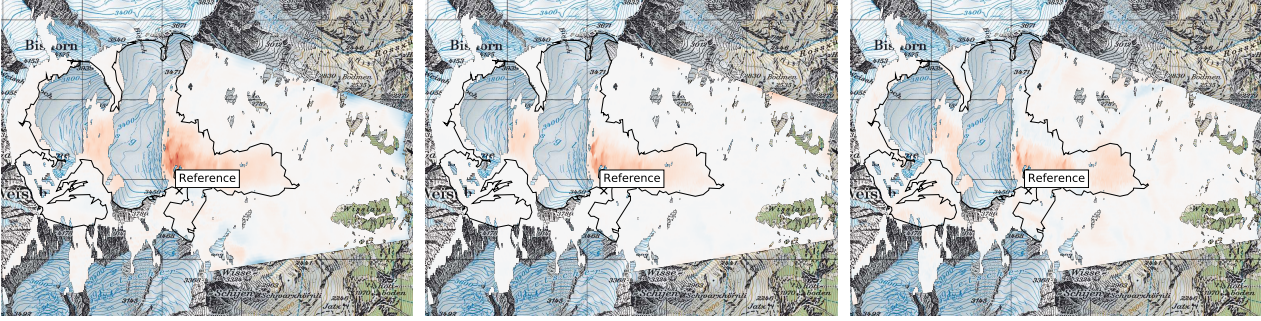
In [41], a single reference interferogram network was considered, where interferograms are computed with respect to one master acquisition, with the purpose of detecting very small displacements. In that case, the scene under study was located at distances between 0 m and 1400 m from the radar; thus the total propagation path is almost 1/8 of the path experienced in the Bisgletscher scenario.

Similar consideration apply to [42], where again the scene under study is located much closer to the radar and interferograms are computed with respect to a single reference acquisition. The scenario considered in [44], [56] is again similar, since a single-reference network is considered and the radar-scene distance is once more significantly smaller than in the Bisgletscher study. A similar scenario is considered in [45], [46].

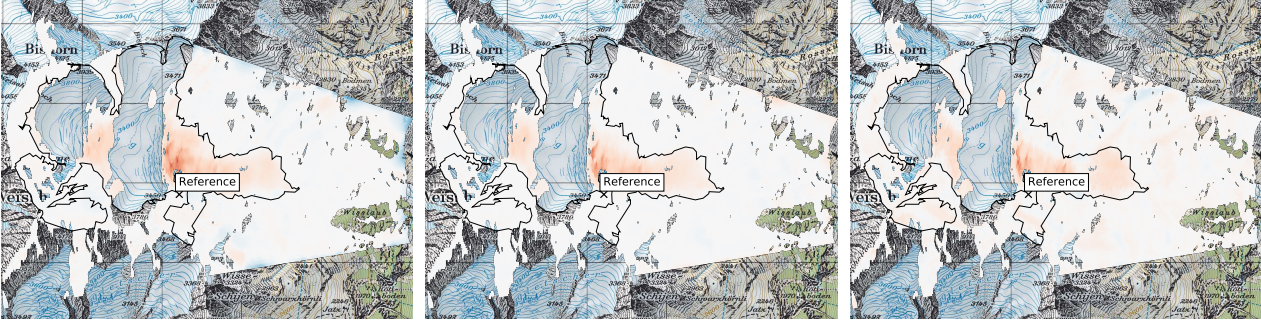
A single-reference interferogram network means that with increasing temporal baselines the effects of global or low-spatial-frequency changes in the atmospheric propagation speed become appreciable. This can be explained as follows: weather-driven changes in the atmospheric water content and especially changes atmospheric pressure—the hydrostatic delay—are presumably of lower spatial frequency compared to the turbulent structures. Moreover, these large scale offset are not likely to vary at the time scale of the radar’s repetition rate, in the order of two minutes for the present case study.



(a) No Spatial APS correction and OLS inversion.



(b) Spatial APS correction using regression-Kriging and OLS inversion.



(c) Spatial APS correction using regression-Kriging and GLS inversion with full covariance model.

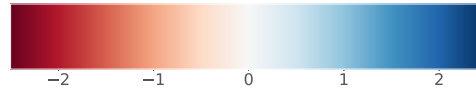
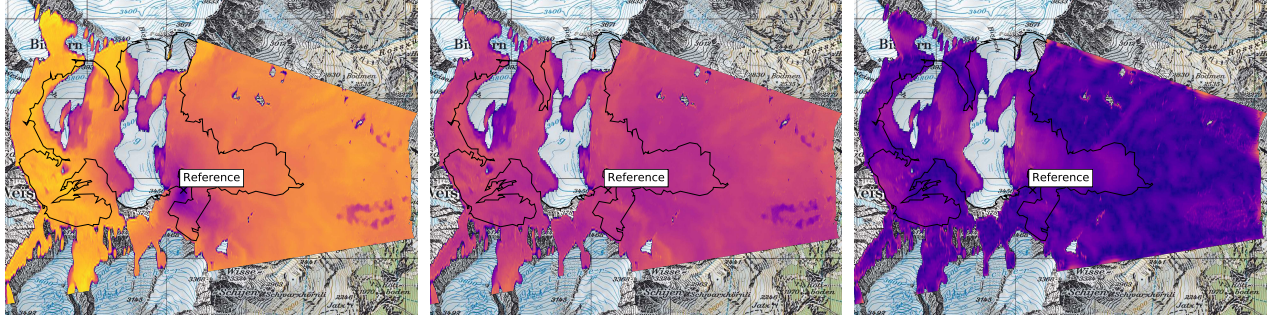
Line of Sight Velocity $\left[\frac{m}{day}\right]$

Fig. 8: time-series of estimated velocity maps for a subset of times. From left to right: July 14 2:33 , July 26 16:32 and August 2 11:36, central European summer time (CEST). (a) no spatial APS correction and OLS solution for the velocity. (b) spatial APS correction using regression-Kriging combined with OLS inversion. (c) spatial APS correction using regression-Kriging and velocity inversion with full covariance model (APS and decorrelation). The outline of Bisgletscher is shown in black. (Basemap: [97], outline: [100]).

Therefore, for short temporal baselines, the magnitude of the phase delay caused by turbulence —mostly associated with turbulent mixing of wet air, the *wet delay*— may be stronger than the stratification signal.

In contrast to these studies, Dematteis [47] computed interferograms between subsequent data takes. He reported a good performance of the stratification model fit; however, the author is using a longer repeat time of 16 min, almost eight times as

large as the one employed in the Bisgletscher observation. In addition to this, the observation geometry is different from the one used in the Bisgletscher campaign. In the former, the radar is looking upwards from a much lower elevation (1500 m) towards the glacier located at higher altitudes, while in the latter the glacier is observed from almost the same elevation as the glacier's center but with the propagation path crossing a valley.

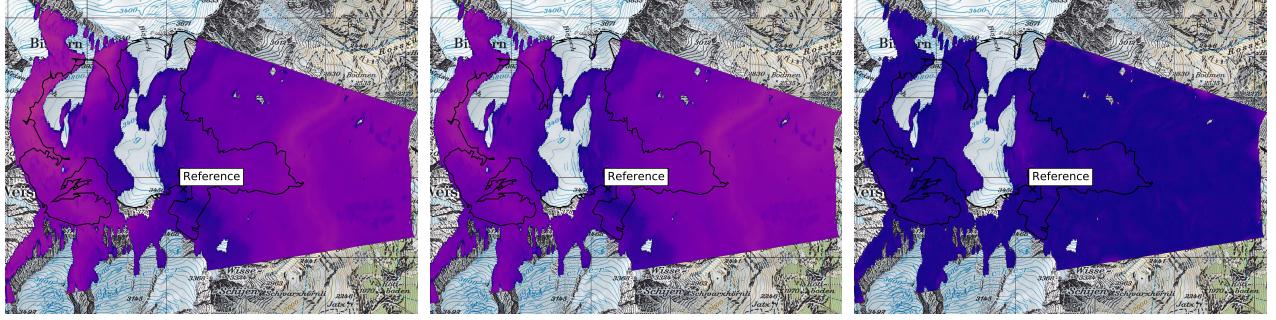


(a) No Spatial APS correction.

(b) Spatial APS correction with stratified model.

(c) Spatial APS correction using regression-Kriging.

The velocity in this group of maps was estimated from individual interferograms.

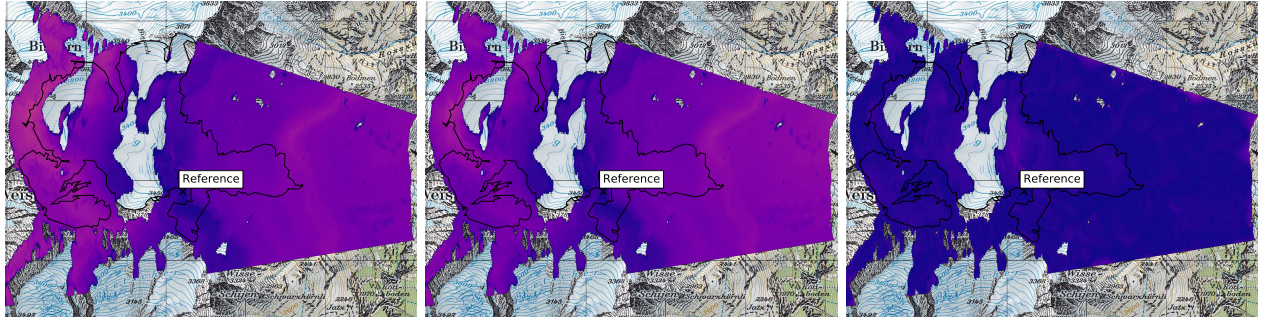


(d)

(e)

(f)

The velocity in this group of maps was estimated using OLS inversion on the corrected interferograms.

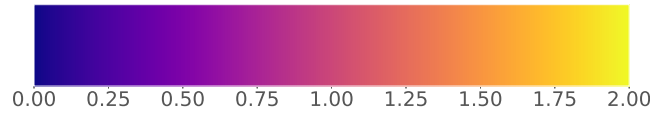


(g)

(h)

(i)

The velocity in this group of maps was estimated with GLS inversion and a temporal covariance model considering APS and decorrelation.



Standard deviation of the estimates LOS velocity [m/day]

Fig. 9: Standard deviation maps of velocity estimates for different combinations of APS correction and velocity inversion methods. From left to right: no correction, stratified APS model, regression-Kriging. From top to bottom: velocities estimated from single interferograms, OLS inversion, GLS inversion with the *APS+Coh* covariance model. (Basemap: [97]).

2) *Covariance Model For Turbulent APS*: In Fig. 5a, the individual spatial variograms obtained from a number of PS interferograms are shown as dots colored by temporal baseline. Under the separable covariance model, increases in the temporal baseline can only scale or offset the spatial variogram but not modify its shape [101].

In the experimental variograms the shape changes with

increasing temporal lags, as shown by the different shapes of the upper and lower range of the standard deviation ribbon plot. With increasing temporal lags, an oscillation in the middle at 2500 m sample separation becomes visible; this type of periodic structure of the variogram is likely a combination of the *hole effect* [102], which is observed for spatially periodic structures, and of anisotropy in the spatial correlation structure

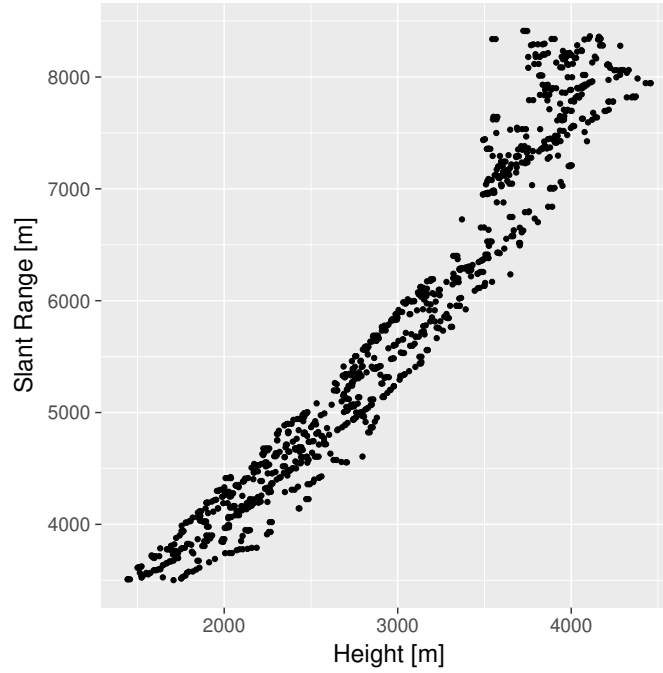


Fig. 10: Scatterplot illustrating the correlation between the slant range (r) and height (h) used as regressors for several models of atmospheric stratification listed in Table I.

of the APS, which was assumed to be isotropic.

Moreover, the variation in spatial variogram shape as a function of temporal lags indicates the possibility of space-time interactions. Given the relatively short repeat interval, it is not surprising that these interactions may happen. A classic example is Taylor’s hypothesis [33], [68] (or the frozen-flow model), where turbulent structures are transported by the wind without changing their shape.

Despite the variability, suggesting some instationarity, a separable covariance model is chosen as an approximation, because of its clear computational advantage. Under this model, only one spatial covariance function needs to be fit to the average of individual spatial variograms. This function can be used to predict the unobserved APS in all interferograms.

The average variogram is shown in the plot as a dashed black line; the blue line shows an exponential variogram fit. The average spatial variogram shows again the same oscillation that was observed in the individual variograms, especially in those at larger temporal lags. This is likely a sign of periodic structures in the APS or of anisotropies. The former could be caused by phase unwrapping error, while the latter suggest that a more comprehensive variogram model including anisotropy could result in a better fit [103], [104].

A more sophisticated approach to spatial covariance modeling has been suggested [75], where instead of stationary, isotropic covariance functions, the author proposed to use intrinsic random functions of order k (IRF-K). This framework permits to estimate non-stationary, anisotropic covariance functions. The authors used this method to extrapolate the observed APS from the PS to the rest of the scene.

However, in the case study presented by Butt, performed on another interferometric time-series of the same Bisgletscher

scene, only an isotropic –albeit instationary– covariance function was used in the interpolation.

3) *Performance of Spatial APS Removal*: The performance of APS prediction and removal using regression-Kriging is evaluated in Fig. 6 in the row named *no* by plotting the histogram of velocity estimates obtained from corrected interferogram pixels on stable areas, as described in subsection II-B.

If no spatial APS correction is applied (column *no*, of Fig. 6 and last row of Table II), a large bias and standard deviation are observed. The latter is almost as high as one half of the expected maximum displacement of the glacier’s surface. Obviously, if no correction of the APS is used, the estimated displacement will be very unreliable.

The large error variance is also visible in the standard deviation map in Fig. 9a. Interestingly, a minimum in standard deviation is observed in the vicinity of the reference point. This is because referencing the phase is able to mitigate some APS contribution by exploiting its spatial correlation.

By subtracting an estimate of the stratified APS (column *lm* of Fig. 6 and second-to-last row of Table II) a reduction in phase variance is visible in comparison to the uncorrected interferograms. However, the standard deviation of the estimates is only reduced by one third, as shown in the summary statistics of Table II. This is also appreciated in Fig. 9b, where the overall variance is reduced. The latter result is consistent with the poor performance of stratified APS model, as no model was capable to explain more than 30 percent of the phase variance of the APS. This is observed in the R^2 plot of Fig. 4b. Thus, most of the observed phase variation it should likely be attributed to the turbulent APS.

Compared to the uncorrected case, the subtraction of the regression-Kriging estimates (column *kriged* of Fig. 6 and row

“kriged, no” Table II) of APS reduces the standard deviation by three quarters.

In the map (c) of Fig. 9, the standard deviation is lower overall: now instead of using a single phase reference as in the uncorrected base case, a set of phase references—the locations of the non-moving PS—is used to extrapolate the APS using the estimated covariance function.

An area of high estimation variance is still observed in the center of the scene, at the location of Bisgletscher. A part of this variance is probably caused by natural variations in the glacier’s surface speed. The remaining variance is likely the inherent regression-Kriging prediction variance, which increases with increasing distance between observations at the PS and reconstruction locations.

Namely, in the case of the glacier, the average distance between pixels on the glacier surface and the nearest PS is larger than in the rest of the scene. A similar pattern was seen in the theoretical variance maps produced by the regression-Kriging procedure.

A similar APS correction performance is observed in the IRF-k approach described by [75]. This result is expected given the fact that intrinsic random functions are comparable to regression-Kriging if the covariance function for the latter is estimated in a manner accounting for the non-stationarity [78], which is partly obtained by removing the stratification trend before variogram estimation.

B. Temporal Inversion

1) *Temporal Covariance Model*: The temporally correlated noise in the interferogram phase vector is modeled as the sum of a residual APS plus the phase noise due to decorrelation. The latter is described with a Brownian motion model, attributed to random motion of many scatterers in each resolution cell, resulting in an exponential decay of the interferometric coherence γ .

The estimated exponential decay parameters are displayed in Fig. 7; a very wide spread of the decorrelation time constant τ is noticeable in Fig. 7b, probably due to the variety of surfaces types, from rocks to forests and glaciated areas. Of particular interest for this analysis is the surface of the glacier, outlined by the polygon.

There, a time constant between 5 min and 2 h is observed. This ensures reliable interferometric phases up to temporal baselines of approximately 1 h for the slower decorrelating areas, assuming a minimum coherence threshold of 0.6. Given the high probability of displacements producing phase wraps, it is not advisable to include interferograms with such large temporal baselines in the time-series inversion.

On the other hand, the spatial variability in the short-term coherence γ_0 , which roughly corresponds to the mean coherence at the shortest temporal baseline of 150 s, is lower (see Fig. 7a). Areas that show a low short-term coherence correspond chiefly to vegetation and regions of low backscatter intensity, while the estimate over the glaciers tongue displays high coherence, suggesting the suitability of the chosen repeat time of 150 s for this study.

The other component of the temporal covariance matrix is represented by the temporally correlated contribution of

the APS, which is estimated by an empirical variogram, as discussed in subsection II-C. The experimental variogram is displayed in Fig. 5b together with an exponential variogram model fit; it appears that the semivariance rapidly increases and settles at 90 percent of the sill after about 500 s, such that after this time the APS can be effectively considered uncorrelated. However, significant variability is observed between variograms computed at different dates (represented as different colors in the plot), presumably reflecting the large variability in propagation conditions related to weather changes.

The rapid settling of the variogram at the sill is in contrast with the observation made by Iannini [56], where the semivariance was observed to increase up to a time lag of 5 days before settling to a sill. The observation conditions were significantly different in that case, since the targets of interest were much closer to the radar (600 m vs 8 km for the Bisgletscher data set) and measurements were performed at lower elevations. Moreover, the variograms in that work were estimated without removing the stratification trends, thus possibly explaining the longer correlation time—up to five days—claimed by the authors.

This result suggests that the APS is not significantly correlated in time at the timescales of the acquisition rate of 2.5 min minutes. Specific experiments—for example by observing a single location at high repeat interval—would be necessary to determine the decorrelation time of the APS.

2) *Performance of Pixel-wise GLS Inversion*: When both components of the temporal covariance matrix are estimated, the inversion for the estimated velocity is performed according to (40). An assessment of inversion quality is made with the same cross-validation method employed to evaluate spatial APS removal, shown in Fig. 6.

All temporal inversion approaches result in a lower variance of residual velocities for stable areas compared to the inversion of the velocity performed on individual interferograms. The differences in performance between temporal covariance models appear not to be significant, with both cases considering either the decorrelation or the APS only showing a very similar residual distribution as the OLS inversion. This is quantified in Table II, where the bias and standard deviation for the *APS+Coh*, *Coh* and *OLS* covariance models are almost identical for all spatial APS correction approaches.

Including the Brownian coherence decay model does not affect estimation standard deviation and bias because these parameters are estimated using cross/validation on a set of PS, which are not affected by temporal decorrelation.

Similarly, including the APS covariance model seems not to significantly reduce the variance of the estimates. This could be explained by the short temporal correlation, as observed in Fig. 5b: after 500 s the semivariance attains a value very close to the sill, implying that the APS between temporally close acquisitions is not significantly correlated. A higher sampling rate—that is shorter acquisition repeat times—is necessary to observe significant temporal correlation, suggesting the potential for future studies.

In the data set analyzed by this paper, including the temporal APS covariance model in the pixel-wise inversion does not

appreciably change the estimation performance. Therefore, the covariance model could be reduced to the one used for spaceborne InSAR [39], where the APS is assumed uncorrelated in time.

An analysis of the general pattern of the estimated LOS velocity fields can be made considering the plots in Fig. 8. In Fig. 8a the velocity maps were generated directly from uncorrected interferograms, by converting the phases into daily displacement velocities.

These maps appear to correctly capture the spatial patterns of motion known from previous optical observations, where the highest velocities were observed at the glacier's tongue and near the upper and lower icefalls. However, a gross overestimation of displacement rates on areas located outside of the glacier—which should not move during the timespan covered by the acquisitions—is observed. The overestimation is presumably caused by the uncompensated APS; this can lead to misinterpretations of the velocity maps.

The overestimation is reduced in Fig. 8c, showing the standard deviation of the estimates obtained by extrapolating the APS using regression-Kriging and then applying the pixel-wise GLS inversion with the *APS+Coherence* covariance model.

Finally, a visualization of the spatial distribution of correction and estimation quality is shown in Fig. 9 in the second and third row, which display the temporal standard deviation of velocity estimates for several combinations of APS correction and covariance models used for the GLS inversion.

As seen in the velocity histograms in Fig. 6, there is no difference in velocity estimation variance across the solution obtained combining regression-Kriging and an OLS inversion (Fig. 9f) and the GLS solution considering the temporal correlation due to the APS and to the decorrelation signal (Fig. 9i). This seems plausible given the short correlation time of the APS, as determined by the means of the temporal variogram in Fig. 5b.

VI. CONCLUSIONS

This paper presents a study on estimation and correction of the atmospheric phase screen (APS) in Ku-Band terrestrial radar interferometry. The APS is one of the most important factors affecting the precision of displacement estimates in radar interferometry. While for spaceborne SAR interferometry a vast literature of approaches for APS modeling and mitigation is available, only few studies are dedicated to the APS in terrestrial radar interferometry.

This study contributes to close this research gap by addressing several aspects of the modeling and correction of APS for terrestrial radar interferometry. To do so, this paper proposes an expansion of the common APS model tailored to TRI. The conventional model—a combination of a stratified atmospheric contribution and of a temporally uncorrelated, spatially correlated stochastic term describing turbulence—is modified by allowing the APS to be correlated in time to account for the short revisit times. To reduce its complexity, the covariance structure of the turbulent component is assumed to be stationary in space and time and separable. Under this assumption, covariance model parameters are fitted by

performing marginal spatial and temporal variogram analysis on a large set of interferograms acquired at different times.

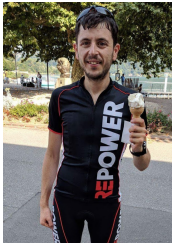
This framework is the foundation of a method for APS correction based on an interferogram stack, from which a set of persistent scatterers unaffected by displacement is determined. The interferometric phase observations at these PS—assumed to contain solely an APS contribution—are used to extrapolate the APS to a regular grid covering the interferograms using regression-Kriging, which accounts for both a model of atmospheric stratification and for the spatial correlation of the atmospheric turbulence. Since separable spatio-temporal statistics are assumed, the interpolation is performed using a single covariance function for the entire stack.

By this method, a phase calibrated stack is obtained, where the residual nuisances, namely unmodeled APS and decorrelation are assumed to be spatially uncorrelated. In this manner, a pixel-wise generalized least squares estimator using the temporal covariance model can be applied to the phase-calibrated stack to estimate displacement rates. This approach reduces the computational load since spatial correlations are assumed to be removed by the preceding Kriging-based APS phase calibration step.

The proposed approach is tested using a Ku-Band radar data set over the Bisele Glacier, southwestern Swiss Alps. Regression analysis using a set of persistent scatterers located on stable areas shows that stratification models have a poor ability to explain a significant portion of the phase variance caused by the APS, highlighting the importance of statistical description of the turbulent APS.

Variogram analysis suggests that a separable spatio-temporal covariance model is a sufficient approximation for the case considered in the study and that the APS only shows a weak correlation in time. The spatial covariance function derived from this analysis is used for the regression-Kriging APS phase calibration, whose performance is evaluated by estimating the residual velocities at locations known not to be affected by displacements.

This analysis shows a significant reduction in phase variance after the regression-Kriging based phase calibration. The same performance analysis is repeated with the output of the time-series inversion applied on the stack of calibrated interferograms. The results show an additional reduction in residual phase variance, at the cost of a coarser temporal resolution caused by the choice of a simplified displacement model.



Simone Baffelli (S'13) received the BSc. and MSc. titles in electrical engineering from the Swiss Federal Institute of Technology (ETH) in Zürich, Switzerland in 2011 and 2013 respectively. He was a doctoral student at the Chair of Earth Observation and Remote Sensing, Swiss Federal Institute of Technology (ETH) in Zürich, Switzerland.

His current research interests include the use of ground based radar systems for the mapping of surface displacement, the analysis and correction of atmospheric phase screen in terrestrial differential

interferometry and the processing, calibration and applications of polarimetric terrestrial radar data.



Othmar Frey (S'04–M'08–SM'17) received the M.Sc. degree in geomatic engineering (Hons.) from ETH Zurich, Zurich, Switzerland, in 2002, and the Ph.D. (Dr. sc. nat.) degree (Hons.) in radar remote sensing from the University of Zurich, in 2010. Othmar Frey is a tenured Senior Researcher and Lecturer at ETH Zurich, Zurich, Switzerland, and also a Senior Scientist at GAMMA Remote Sensing AG, Gümliigen, Switzerland. He has been working in this joint academic/industry setting since 2011. Previously, from 2002 to 2010, he was a Research

Associate with the Remote Sensing Laboratories, University of Zurich. His research encompasses 2-D and 3-D (tomographic) synthetic aperture radar (SAR) focusing techniques and interferometric techniques for applications such as 3-D forest mapping, ground deformation monitoring (persistent scatterer interferometry / differential tomography), and profiling the structure of snowpacks, using spaceborne, airborne, and terrestrial radar sensors. He has been active in various national and international research projects, as a PI and project manager as well as a co-investigator. At GAMMA he has also been active in the development of the Gamma Software and in technical consulting related to SAR imaging and interferometric applications. He has been a member of the SAOCOM-CS Science Expert Group with the European Space Agency. Since 2015, he has been the chair of the Swiss Chapter of the IEEE Geoscience and Remote Sensing Society. Dr. Frey received the distinction award and prize of the Faculty of Science, University of Zurich, for his Ph.D. thesis, in 2010, and he received the ETH medal for an outstanding M.Sc. thesis, in 2002. He was the recipient of the 3rd Place Student Paper Award at the 2010 EUSAR Conference in Aachen, Germany, and he was a co-recipient of the Best Paper Award at the ISPRS Workshop Laserscanning and Silvilaser 2007 in Helsinki, Finland.



Irena Hajnsek (A'01 – M'06 – SM'09 – F'14) received the Dipl. Degree (Honors) from the Free University of Berlin, Berlin, Germany, in 1996 and the Dr. degree (Honors) from the Friedrich Schiller University Jena, Jena, Germany, in 2001. Since November 2009, she has been a Professor of Earth observation with the Institute of Environmental Engineering, Swiss Federal Institute of Technology (ETH) Zurich, Zurich, Switzerland, and, at the same time, the Head of the Polarimetric SAR Interferometry Group, Microwaves and Radar Institute (HR),

German Aerospace Center (DLR), Wessling, Germany. From 1996 to 1999, she was with the DLR-HR. From 1999 to 2000, she was with the Institut d'Electronique et de Telecommunications de Rennes, University of Rennes 1, Rennes, France for ten months, in the frame of the EC-TMR Radar Polarimetry Network. In 2005, she was a Guest Scientist with the University of Adelaide, Adelaide, Australia, for six weeks. She is the Science Coordinator of the German satellite mission TanDEM-X. Her main research interests are in electromagnetic propagation and scattering theory, radar polarimetry, SAR and interferometric SAR data processing techniques, and environmental parameter modeling and estimation. Dr. Hajnsek was a member of the ESA Mission Advisory Group of the 7th Explorer Mission CoReH2O from 2009 to 2013. She was a Technical Program Cochair of the 2012 IEEE International Geoscience and Remote Sensing Symposium in Munich. Since 2013, she has been a member of the IEEE Geoscience and Remote Sensing Society Administrative Committee.

REFERENCES

- [1] J. Faillettaz, M. Funk, and C. Vincent, "Avalanching glacier instabilities: review on processes and early warning perspectives," *Reviews of Geophysics*, vol. 53, pp. 203–224, 2015.
- [2] A. Pralong and M. Funk, "On the instability of avalanching glaciers," *Journal of Glaciology*, vol. 52, pp. 31–48, 2006.
- [3] H. Röthlisberger and P. Kasser, "Gletscher und klima—glaciers et climat, jahrbuch der schweizerischen naturforschenden gesellschaft, wissenschaftlicher teil 1978," 1981.
- [4] W. Haeberli, C. Huggel, A. Kääb, S. Zraggen-Oswald, A. Polkvoj, I. Galushkin, I. Zotikov, and N. Osokin, "The kolka-karmadon rock/ice slide of 20 september 2002: an extraordinary event of historical dimensions in north ossetia, russian caucasus," *Journal of Glaciology*, vol. 50, no. 171, pp. 533–546, 2004.
- [5] A. Flotron, "Movement studies on a hanging glacier in relation with an ice avalanche," *Journal of Glaciology*, vol. 19, pp. 671–672, Jan. 1977.
- [6] J. Faillettaz, A. Pralong, M. Funk, and N. Deichmann, "Evidence of log-periodic oscillations and increasing icequake activity during the breaking-off of large ice masses," *Journal of Glaciology*, vol. 54, pp. 725–737, Dec. 2008.
- [7] H. Röthlisberger, "Sliding phenomena in a steep section of Balmhornletscher, Switzerland," *Journal of Geophysical Research*, vol. 92, p. 8999, 1987.
- [8] P. D. Canassy, J. Faillettaz, F. Walter, and M. Huss, "Seismic activity and surface motion of a steep temperate glacier: a study on Triftgletscher, Switzerland," *Journal of Glaciology*, vol. 58, pp. 513–528, 2012.
- [9] G. Luzi, M. Pieraccini, D. Mecatti, L. Noferini, G. Macaluso, A. Tamburini, and C. Atzeni, "Monitoring of an alpine glacier by means of ground-based SAR interferometry," *IEEE Geoscience and Remote Sensing Letters*, vol. 4, pp. 495–499, Jul. 2007.
- [10] A. Kääb, R. Wessels, W. Haeberli, C. Huggel, J. S. Kargel, and S. J. S. Khalsa, "Rapid ASTER imaging facilitates timely assessment of glacier hazards and disasters," *Eos, Transactions American Geophysical Union*, vol. 84, p. 117, 2003.
- [11] A. Kääb, C. Huggel, L. Fischer, S. Guex, F. Paul, I. Roer, N. Salzmann, S. Schlaefli, K. Schmutz, D. Schneider, T. Strozzi, and Y. Weidmann, "Remote sensing of glacier- and permafrost-related hazards in high mountains: an overview," *Natural Hazards and Earth System Sciences*, vol. 5, pp. 527–554, 2005.
- [12] E. Berthier, H. Vadon, D. Baratoux, Y. Arnaud, C. Vincent, K. Feigl, F. Rémy, and B. Legrésy, "Surface motion of mountain glaciers derived from satellite optical imagery," *Remote Sensing of Environment*, vol. 95, pp. 14–28, 2005.
- [13] A. Kääb, "Monitoring high-mountain terrain deformation from repeated air- and spaceborne optical data: examples using digital aerial imagery and ASTER

- data,” *ISPRS Journal of Photogrammetry and Remote Sensing*, vol. 57, pp. 39–52, 2002.
- [14] T. A. Scambos, M. J. Dutkiewicz, J. C. Wilson, and R. A. Bindenschadler, “Application of image cross-correlation to the measurement of glacier velocity using satellite image data,” *Remote Sensing of Environment*, vol. 42, pp. 177–186, 1992.
- [15] R. M. Goldstein, H. Engelhardt, B. Kamb, and R. M. Frolich, “Satellite radar interferometry for monitoring ice sheet motion: application to an antarctic ice stream,” *Science*, vol. 262, pp. 1525–1530, 1993.
- [16] A. Gray, N. Short, K. Mattar, and K. Jezek, “Velocities and flux of the Filchner ice shelf and its tributaries determined from speckle tracking interferometry,” *Canadian Journal of Remote Sensing*, vol. 27, pp. 193–206, 2001.
- [17] T. Strozzi, A. Luckman, T. Murray, U. Wegmüller, and C. Werner, “Glacier motion estimation using SAR offset-tracking procedures,” *IEEE Transactions on Geoscience and Remote Sensing*, vol. 40, pp. 2384–2391, 2002.
- [18] I. Joughin, R. Kwok, and M. Fahnestock, “Estimation of ice-sheet motion using satellite radar interferometry: method and error analysis with application to Humboldt Glacier, Greenland,” *Journal of Glaciology*, vol. 42, pp. 564–575, Jan. 1996.
- [19] B. T. Rabus and D. R. Fatland, “Comparison of SAR-interferometric and surveyed velocities on a mountain glacier: Black Rapids Glacier, Alaska, U.S.A.,” *Journal of Glaciology*, vol. 46, pp. 119–128, 2000.
- [20] R. Michel and E. Rignot, “Flow of Glaciar Moreno, Argentina, from repeat-pass Shuttle Imaging Radar images: comparison of the phase correlation method with radar interferometry,” *Journal of Glaciology*, vol. 45, pp. 93–100, 1999.
- [21] K. E. Allstadt, D. E. Shean, A. Campbell, M. Fahnestock, and S. D. Malone, “Observations of seasonal and diurnal glacier velocities at Mount Rainier, Washington, using terrestrial radar interferometry,” *Cryosphere*, vol. 9, pp. 2219–2235, 2015.
- [22] D. Voytenko, T. H. Dixon, I. M. Howat, N. Gourmelen, C. Lembke, C. L. Werner, S. D. L. Peña, and B. Oddsson, “Multi-year observations of Breiðamerkurjökull, a marine-terminating glacier in southeastern Iceland, using terrestrial radar interferometry,” *Journal of Glaciology*, vol. 61, pp. 42–54, 2015.
- [23] T. H. Dixon, D. Voytenko, C. Lembke, S. de la Peña, I. Howat, N. Gourmelen, C. Werner, and B. Oddsson, “Emerging technology monitors ice-sea interface at outlet glaciers,” *Eos*, vol. 93, pp. 497–498, 2012.
- [24] L. Noferini, D. Mecatti, G. Macaluso, M. Pieraccini, and C. Atzeni, “Monitoring of Belvedere Glacier using a wide angle GB-SAR interferometer,” *Journal of Applied Geophysics*, vol. 68, pp. 289–293, 2009.
- [25] D. Mecatti, L. Noferini, G. Macaluso, M. Pieraccini, G. Luzi, C. Atzeni, and A. Tamburini, “Remote sensing of glacier by ground-based radar interferometry,” in *Proceedings of the IEEE International Geoscience and Remote Sensing Symposium*, IEEE, 2007, pp. 4501–4504.
- [26] D. Massonnet and K. L. Feigl, “Radar interferometry and its application to changes in the earth’s surface,” *Reviews of Geophysics*, vol. 36, pp. 441–500, 1998.
- [27] M. Bevis, S. Businger, T. A. Herring, C. Rocken, R. A. Anthes, and R. H. Ware, “GPS meteorology: remote sensing of atmospheric water vapor using the global positioning system,” *Journal of Geophysical Research*, vol. 97, p. 15 787, 1992.
- [28] R. F. Hanssen, “Atmospheric heterogeneities in ERS tandem SAR interferometry,” Delft University, Tech. Rep., 1998.
- [29] R. N. Treuhaft and G. E. Lanyi, “The effect of the dynamic wet troposphere on radio interferometric measurements,” *Radio Science*, vol. 22, pp. 251–265, Mar. 1987.
- [30] R. F. Hanssen, *Radar Interferometry*, ser. Remote Sensing and Digital Image Processing. Springer Netherlands, Feb. 2001, vol. 2, pp. 46–53.
- [31] J. Jung, D. jin Kim, and S.-E. Park, “Correction of atmospheric phase screen in time series InSAR using WRF model for monitoring volcanic activities,” *IEEE Transactions on Geoscience and Remote Sensing*, vol. 52, pp. 2678–2689, 2014.
- [32] T. R. Emardson, M. Simons, and F. H. Webb, “Neutral atmospheric delay in interferometric synthetic aperture radar applications: statistical description and mitigation,” *Journal of Geophysical Research: Solid Earth*, vol. 108, p. 2231, 2003.
- [33] F. Onn and H. A. Zebker, “Correction for interferometric synthetic aperture radar atmospheric phase artifacts using time series of zenith wet delay observations from a GPS network,” *Journal of Geophysical Research: Solid Earth*, vol. 111, pp. 1–16, 2006.
- [34] S. Williams, Y. Bock, and P. Fang, “Integrated satellite interferometry: tropospheric noise, GPS estimates and implications for interferometric synthetic aperture radar products,” *Journal of Geophysical Research: Solid Earth*, vol. 103, pp. 27 051–27 067, Nov. 1998.
- [35] P. Basili, S. Bonafoni, V. Mattioli, P. Ciotti, and N. Pierdicca, “Mapping the atmospheric water vapor by integrating microwave radiometer and GPS measurements,” *IEEE Transactions on Geoscience and Remote Sensing*, vol. 42, pp. 1657–1665, 2004.
- [36] Z. Li, J.-P. Muller, P. Cross, P. Albert, J. Fischer, and R. Bennartz, “Assessment of the potential of MERIS near-infrared water vapour products to correct ASAR interferometric measurements,” *International Journal of Remote Sensing*, vol. 27, pp. 349–365, Jan. 2006.
- [37] Z. W. Li, W. B. Xu, G. C. Feng, J. Hu, C. C. Wang, X. L. Ding, and J. J. Zhu, “Correcting atmospheric effects on InSAR with MERIS water vapour data and elevation-dependent interpolation model,” *Geophysical Journal International*, vol. 189, pp. 898–910, 2012.
- [38] Z. Li, E. J. Fielding, P. Cross, and R. Preusker, “Advanced InSAR atmospheric correction: MERIS/MODIS combination and stacked water

- vapour models,” *International Journal of Remote Sensing*, vol. 30, pp. 3343–3363, 2009.
- [39] P. S. Agram and M. Simons, “A noise model for InSAR time series,” *Journal of Geophysical Research: Solid Earth*, pp. 1–20, 2015.
- [40] R. Jolivet, P. S. Agram, N. Y. Lin, M. Simons, M.-P. Doin, G. Peltzer, and Z. Li, “Improving InSAR geodesy using global atmospheric models,” *Journal of Geophysical Research: Solid Earth*, vol. 119, pp. 2324–2341, 2014.
- [41] L. Pipia, X. Fabregas, A. Aguasca, and C. Lopez-Martinez, “Atmospheric artifact compensation in ground-based DInSAR applications,” *IEEE Geoscience and Remote Sensing Letters*, vol. 5, pp. 88–92, Jan. 2008.
- [42] L. Noferini, M. Pieraccini, D. Mecatti, G. Luzi, C. Atzeni, A. Tamburini, and M. Broccolato, “Permanent scatterers analysis for atmospheric correction in ground-based SAR interferometry,” *IEEE Transactions on Geoscience and Remote Sensing*, vol. 43, pp. 1459–1471, 2005.
- [43] G. Luzi, M. Pieraccini, D. Mecatti, L. Noferini, G. Guidi, F. Moia, and C. Atzeni, “Ground-based radar interferometry for landslides monitoring: atmospheric and instrumental decorrelation sources on experimental data,” *IEEE Transactions on Geoscience and Remote Sensing*, vol. 42, pp. 2454–2466, 2004.
- [44] A. M. Guarnieri, L. Iannini, and D. Giudici, “On the exploitation of meteo information for atmospheric phase screen compensation in GB-SAR interferometry,” in *ESA Living Planet Symposium*, 2010.
- [45] R. Iglesias, X. Fabregas, A. Aguasca, J. J. Mallorqui, C. Lopez-Martinez, J. A. Gili, and J. Corominas, “Atmospheric phase screen compensation in ground-based SAR with a multiple-regression model over mountainous regions,” *IEEE Transactions on Geoscience and Remote Sensing*, vol. 52, pp. 2436–2449, 2014.
- [46] R. Iglesias, A. Aguasca, X. Fabregas, J. J. Mallorqui, D. Monells, C. Lopez-Martinez, and L. Pipia, “Ground-based polarimetric SAR interferometry for the monitoring of terrain displacement phenomena—part I: theoretical description,” *IEEE Journal of Selected Topics in Applied Earth Observations and Remote Sensing*, vol. 8, pp. 1–1, 2014.
- [47] N. Dematteis, G. Luzi, D. Giordan, F. Zucca, and P. Allasia, “Monitoring alpine glacier surface deformations with GB-SAR,” *Remote Sensing Letters*, vol. 8, pp. 947–956, 2017.
- [48] P. Webley, G. Wadge, and I. James, “Determining radio wave delay by non-hydrostatic atmospheric modelling of water vapour over mountains,” *Physics and Chemistry of the Earth, Parts A/B/C*, vol. 29, pp. 139–148, 2004.
- [49] J. M. Boncori and J. Mohr, “Statistical description of tropospheric delay for InSAR: overview and a new model,” in *2007 IEEE International Geoscience and Remote Sensing Symposium*, IEEE, 2007, pp. 4483–4486.
- [50] A. Ferretti, C. Prati, and F. Rocca, “Permanent scatterers in SAR interferometry,” *IEEE Transactions on Geoscience and Remote Sensing*, vol. 39, pp. 8–20, 2001.
- [51] C. Werner, U. Wegmüller, T. Strozzi, and A. Wiesmann, “Interferometric point target analysis for deformation mapping,” in *Proceeding of the IEEE International Geoscience and Remote Sensing Symposium*, vol. 7, IEEE, 2003, pp. 4362–4364.
- [52] M. Crosetto, O. Monserrat, M. Cuevas-González, N. Devanthery, and B. Crippa, “Persistent scatterer interferometry: a review,” *ISPRS Journal of Photogrammetry and Remote Sensing*, vol. 115, pp. 78–89, 2016.
- [53] D. G. Krige, “A statistical approach to some basic mine valuation problems on the Witwatersrand,” *Journal of the Chemical, Metallurgical and Mining Society of South Africa*, pp. 201–215, 1952.
- [54] A. Ferretti, C. Prati, and F. Rocca, “Nonlinear subsidence rate estimation using permanent scatterers in differential SAR interferometry,” *IEEE Transactions on Geoscience and Remote Sensing*, vol. 38, pp. 2202–2212, 2000.
- [55] A. Hooper, H. Zebker, P. Segall, and B. Kampes, “A new method for measuring deformation on volcanoes and other natural terrains using InSAR persistent scatterers,” *Geophysical Research Letters*, vol. 31, Dec. 2004.
- [56] L. Iannini and A. Monti Guarnieri, “Atmospheric phase screen in ground-based radar: Statistics and compensation,” *IEEE Geoscience and Remote Sensing Letters*, vol. 8, pp. 537–541, 2011.
- [57] D. Massonnet and T. Rabaute, “Radar interferometry: limits and potential,” *IEEE Transactions on Geoscience and Remote Sensing*, vol. 31, pp. 455–464, Mar. 1993.
- [58] P. Rosen, S. Hensley, I. Joughin, F. Li, S. Madsen, E. Rodriguez, and R. Goldstein, “Synthetic aperture radar interferometry,” *Proceedings of the IEEE*, vol. 88, pp. 333–382, Mar. 2000.
- [59] P. Berardino, G. Fornaro, R. Lanari, and E. Sansosti, “A new algorithm for surface deformation monitoring based on small baseline differential SAR interferograms,” *IEEE Transactions on Geoscience and Remote Sensing*, vol. 40, pp. 2375–2383, Nov. 2002.
- [60] R. Lanari, F. Casu, M. Manzo, G. Zeni, P. Berardino, M. Manunta, and A. Pepe, “An overview of the small Baseline subset algorithm: a DInSAR technique for surface deformation analysis,” in *Pure and Applied Geophysics*, vol. 164, Springer Nature, 2007, pp. 637–661.
- [61] R. Snieder and J. Trampert, “Inverse problems in geophysics,” in *Wavefield Inversion*, Springer Vienna, 1999, pp. 119–190.
- [62] A. Tarantola and B. Valette, “Inverse problems - quest for information,” *Journal of Geophysics*, pp. 159–170, 1982.
- [63] B. M. Kampes, *Radar interferometry*. Springer Netherlands, 2006.

- [64] H. Zebker and J. Villasenor, "Decorrelation in interferometric radar echoes," *IEEE Transactions on Geoscience and Remote Sensing*, vol. 30, pp. 950–959, Sep. 1992.
- [65] R. Touzi, A. Lopes, J. Bruniquel, and P. Vachon, "Coherence estimation for SAR imagery," *IEEE Transactions on Geoscience and Remote Sensing*, vol. 37, pp. 135–149, 1999.
- [66] E. Rodriguez and J. Martin, "Theory and design of interferometric synthetic aperture radars," *IEE Proceedings F Radar and Signal Processing*, vol. 139, p. 147, 1992.
- [67] F. Rocca, "Modeling interferogram stacks," *IEEE Transactions on Geoscience and Remote Sensing*, vol. 45, pp. 3289–3299, Oct. 2007.
- [68] T. Gneiting, M. Genton, and P. Guttorp, "Geostatistical Space-Time Models, Stationarity, Separability, and Full Symmetry," in *Statistical Methods for Spatio-Temporal Systems*, Chapman and Hall, Oct. 2006, pp. 151–175.
- [69] V. K. Gupta and E. Waymire, "On Taylor's hypothesis and dissipation in rainfall," *Journal of Geophysical Research*, vol. 92, p. 9657, 1987.
- [70] R. F. Hanssen, "High-resolution water vapor mapping from interferometric radar measurements," *Science*, vol. 283, pp. 1297–1299, 1999.
- [71] M. G. Genton, "Separable approximations of space-time covariance matrices," *Environmetrics*, vol. 18, pp. 681–695, Nov. 2007.
- [72] R. S. Bivand, E. J. Pebesma, and V. Gómez-Rubio, "Applied spatial data analysis with R," in *Use R*, vol. 1, Springer New York, 2013, p. 378.
- [73] W. H. Greene, "The generalized regression model and heteroscedasticity," in *Econometric Analysis*, 7th ed. Pearson, 2010, ch. 9.
- [74] H. Wackernagel, *Multivariate Geostatistics*. Springer, 2003.
- [75] J. Butt, A. Wieser, and S. Conzett, "Intrinsic random functions for mitigation of atmospheric effects in terrestrial radar interferometry," *Proceedings of JISDM 2016 Vienna*, vol. 11, pp. 89–98, 2016.
- [76] G. Matheron, *The Intrinsic Random Functions and Their Applications*, 1973.
- [77] K. G. van den Boogaart and A. Brenning, "Why universal Kriging is better than IRFk-Kriging : estimation of variograms in the presence of trend," *Journal of Earth System Science*, pp. 1–15, 2001.
- [78] R. Christensen, "The equivalence of predictions from universal Kriging and intrinsic random-function Kriging," *Mathematical Geology*, vol. 22, pp. 655–664, 1990.
- [79] N. Blaunstein and C. Christodoulou, *Radio Propagation and Adaptive Antennas for Wireless Communication Links*, ser. Wiley Series in Microwave and Optical Engineering. John Wiley & Sons, Inc., Nov. 2006, vol. 8, ch. 6.
- [80] H. Akaike, "A new look at the statistical model identification," *IEEE Transactions on Automatic Control*, vol. 19, pp. 716–723, 1974.
- [81] H. A. Zebker, P. A. Rosen, and S. Hensley, "Atmospheric effects in interferometric synthetic aperture radar surface deformation and topographic maps," *Journal of Geophysical Research: Solid Earth*, vol. 102, pp. 7547–7563, 1997.
- [82] P. Legendre and L. Legendre, "Spatial analysis," in *Numerical ecology 2nd English Edition*, Elsevier, Ed. 1998, pp. 712–738.
- [83] N. Bliznyuk, R. J. Carroll, M. G. Genton, and Y. Wang, "Variogram estimation in the presence of trend," *Statistics and Its Interface*, vol. 5, pp. 159–168, Dec. 2012.
- [84] R. Caduff, A. Kos, F. Schlunegger, B. W. McArdell, and A. Wiesmann, "Terrestrial radar interferometric measurement of hillslope deformation and atmospheric disturbances in the Illgraben debris-flow catchment, Switzerland," *IEEE Geoscience and Remote Sensing Letters*, vol. 11, pp. 434–438, Feb. 2014.
- [85] L. Kristensen, C. Rivolta, J. Dehls, and L. H. Blikra, "GB InSAR measurement at the Åknes rockslide, Norway," *Italian Journal of Engineering Geology and Environment*, vol. 2013, pp. 339–348, 2013.
- [86] S. Tebaldini and A. Monti, "Methods and performances for multi-pass SAR interferometry," in *Geoscience and Remote Sensing New Achievements*, In-Tech, 2010, pp. 329–357.
- [87] R. Caduff, F. Schlunegger, A. Kos, and A. Wiesmann, "A review of terrestrial radar interferometry for measuring surface change in the geosciences," *Earth Surface Processes and Landforms*, vol. 40, pp. 208–228, Feb. 2015.
- [88] P. Riesen, T. Strozzi, A. Bauder, A. Wiesmann, and M. Funk, "Short-term surface ice motion variations measured with a ground-based portable real aperture radar interferometer," *Journal of Glaciology*, vol. 57, pp. 53–60, 2011.
- [89] J. Biggs, T. Wright, Z. Lu, and B. Parsons, "Multi-interferogram method for measuring interseismic deformation: Denali fault, Alaska," *Geophysical Journal International*, vol. 170, pp. 1165–1179, 2007.
- [90] S. Samiei-Esfahany, J. E. Martins, F. van Leijen, and R. F. Hanssen, "Phase estimation for distributed scatterers in InSAR stacks using integer least squares estimation," *IEEE Transactions on Geoscience and Remote Sensing*, vol. 54, pp. 5671–5687, Oct. 2016.
- [91] T. Strozzi, U. Wegmüller, C. Werner, and A. Wiesmann, "Measurement of slow uniform surface displacement with mm/year accuracy," in *Proceedings of the IEEE International Geoscience and Remote Sensing Symposium*, vol. 00, IEEE, 2000, pp. 4–6.
- [92] S. Baffelli, O. Frey, and I. Hajnsek, "System characterization and polarimetric calibration of the Ku-band advanced polarimetric interferometer," in *Proceedings of the European Conference on Synthetic Aperture Radar*, 2016, pp. 2–5.

- [93] S. Baffelli, O. Frey, C. Werner, and I. Hajnsek, "Polarimetric calibration of the Ku-band advanced polarimetric radar interferometer," *IEEE Transactions on Geoscience and Remote Sensing*, vol. 56, pp. 1–17, Apr. 2018.
- [94] C. L. Werner, A. Wiesmann, T. Strozzi, A. Kos, R. Caduff, and U. Wegmüller, "The GPRI multi-mode differential interferometric radar for ground-based observations," in *Proceedings of the European Conference on Synthetic Aperture Radar*, VDE, 2012, pp. 304–307.
- [95] A. Stove, "Linear FMCW radar techniques," *IEE Proceedings F Radar and Signal Processing*, vol. 139, p. 343, Oct. 1992.
- [96] J. Beutel, B. Buchli, F. Ferrari, M. Keller, M. Zimmerling, and L. Thiele, "X-SENSE: sensing in extreme environments," in *Design, Automation & Test in Europe*, IEEE, Mar. 2011, pp. 1–6.
- [97] Federal Office For Topography (Swisstopo). (). National map 1:50'000, [Online]. Available: [https://www.geocat.ch/geonetwork/srv/ger/md.viewer#/full_view/4c8c7c58-61c7-4a61-8e7a-6ffb95d183df/tab/complete].
- [98] U. Wegmüller, O. Frey, and C. L. Werner, "Point density reduction in persistent scatterer interferometry," in *Proceedings of the European Conference on Synthetic Aperture Radar*, 2012, pp. 673–676.
- [99] P. Di Tommaso, M. Chatzou, E. W. Floden, P. P. Barja, E. Palumbo, and C. Notredame, "Nextflow enables reproducible computational workflows," *Nature Biotechnology*, vol. 35, pp. 316–319, Apr. 2017.
- [100] Federal Office For Topography (Swisstopo). (). Geographical names swissNAMES3D, [Online]. Available: [<https://www.geocat.ch/geonetwork/srv/ita/catalog.search#/metadata/ab24e5cc-7f53-451a-820a-f113fa545943>].
- [101] D. Myers, "Estimating and modeling space-time variograms," in *Proceedings of the joint meeting of The 6th International Symposium On Spatial Accuracy Assessment In Natural Resources and Environmental Sciences and The 15th Annual Conference of The International Environmetrics Society*, 2004.
- [102] E. Gringarten and C. V. Deutsch, "Teacher's aide variogram interpretation and modeling," *Mathematical Geology*, vol. 33, no. 4, pp. 507–534, 2001.
- [103] A. Refice, A. Belmonte, F. Bovenga, and G. Pasquariello, "On the use of anisotropic covariance models in estimating atmospheric DInSAR contributions," *IEEE Geoscience and Remote Sensing Letters*, vol. 8, pp. 341–345, 2011.
- [104] S. Knospe and S. Jonsson, "Covariance estimation for dInSAR surface deformation measurements in the presence of anisotropic atmospheric noise," *IEEE Transactions on Geoscience and Remote Sensing*, vol. 48, no. 4, pp. 2057–2065, 2010.